

Author response to the comments of the Referee Dr.Eigil Kaas.

First of all, we would like to warmly thank Dr. Kaas for his very helpful comments and further advises regarding their implementation. These allowed us to improve the paper, in particular, adding several new directions in the model evaluation and comparison with other approaches. Below, we provide a point-by-point response to the comments.

The Word file with all changes tracked is given as a Supplementary zip archive.

General comments

*A main issue is the numerical accuracy. Probably it is rather difficult to perform an analytic von Neuman analysis with calculation of amplification factors etc. However, this can easily be (and should be) done numerically for different harmonic wave numbers using different time steps (and fft's back and forth). Such an analysis should include a comparison with a known scheme, i.e., a classical semi-Lagrangian scheme with cubic interpolation.*

Thank you for this suggestion and advises on its implementation! We added a section with the numerical spectral analysis and comparison with two classic schemes: the semi-Lagrangian and the Bott algorithms. The new section is 4.5.

*The scheme has some tendency to introduce anti-diffusion for certain shapes and a smoother is therefore introduced in a rather non rigorous way (equation 20). This smoothing seems important in order to obtain reasonable results. However, the nature of the smoother is rather unusual and a more detailed analysis of its performance is requested. In particular it must be clarified in a quantitative way why the value of  $k$  is set to approximately 0.08. What is the exact value that is used in the different runs (hopefully the same value in all runs)?*

We certainly used the same value in all runs with the smoother, the tests can only be with or without it. The paper is now modified with explicit references to whether the smoother was used or not.

We also expanded its description in section 4.4, put explicit analysis of its impact and optimal strength in spectral analysis section and in all tests where it was used. Finally, we added a new section 7.3 in Discussion, where outlined the cases requiring its application.

The idea of the smoother came from the qualitative observation that the scheme with mass centres fixed in the middle of the grid cells is quite similar to a simple upwind algorithm, which is very diffusive and thus has no gradient-sharpening tendencies. The relaxation towards this scheme was

then suggested as a way to counter the anti-diffusivity. The idea is particularly tempting because the additional costs are completely negligible. Specific value of the relaxation factor has been found from numerical tests, which also confirmed its stability in a variety of cases. The actual value of 0.08 was found as the lowest distortion that damps the anti-diffusion in the tests leading to practically non-distorted gradients. In spectral analysis, this corresponds to lowering the amplification factor below 1 for (almost) all wave numbers at (almost) all times.

*As far as I can judge, the scheme has similarities to the CIP and CIP-CLSR schemes by Xiao and others - see below under Specific comments.*

We have added the scheme to the introduction, and drew attention to the generic idea behind the whole class of such schemes: to use "something" that would allow for higher resolution than the formal grid cell size. Apart from this general idea, the similarities seem to be quite limited, less significant than with, e.g. the Egan & Makhoney scheme. The CSLR takes rational functions for describing the within-cell concentration profile. However, there are no slabs and centres of masses, which are the corner stone of the Galperin's approach. Instead, CSLR used concentrations at the interface points to define the profiles. This brings about another principal difference: the interface points are affected by two neighbouring cells, while in Galperin's approach each cell completely decides on its slab when it is formed. The information is passed only with the transported mass.

#### Specific comments

*l. 146 Units are not just mol or kg but mol/kg and kg/kg since they represent mixing ratios.*

In fact, the model operates with masses in the grid cells and, for chemistry, with concentrations, but mmr is, indeed, mol/kg and kg/kg. Clarification added.

*l. 159 "The Eq. (1)" should be replaced by "Eq. (1)"*

*l. 173 "Eulerian dynamics of SILAM". It is proposed to change this to "Eulerian transport scheme of SILAM". Otherwise the reader may be confused to think that the scheme is used for the atmospheric dynamics (on-line coupling), which is not the case.*

*l. 186 "The Eq. (5)" should be replaced by "Eq. (5)"*

*l. 205 "in the Eq. ( 5)" should be replaced by "in Eq. (5)"*

*l. 291 "In application to Galperin scheme" should be "For application to the Galperin scheme" or "For application in the Galperin scheme"*

*Figure 2 It is disturbing that the legends overlap the figures. Please, use one common legend, e.g., between the two upper and two lower panels. Also, in the caption "Legend includes ..." should be replaced with "The Legend includes ...".*

All the deficiencies have been corrected

*l. 253 In my opinion the review of similar schemes is not complete without a discussion of the CIP-CLSR scheme by Xiao (2002). In its essence this scheme is quite similar to the new scheme presented in the manuscript. In CIP, the total field is represented by the cell averages as well as the interphase values between cells. In this way the interphase values play the same role as the center of mass locations in the Galperin scheme. .... Thus, a careful discussion of the essential difference between CIP / CIP-CLSR and the new scheme is requested.*

We included the references to the introduction. Please see above remarks on the schemes similarity.

*l. 320-334 Apparently the Galperin scheme is somehow antidiffusive - although not for all shapes. The distortions seem to be a rather serious issue. The smoothing effectively introduced via the expression in eq. (20) seems, as also noted by the authors, to be a non-rigorous fix. It is, however, obvious that the numerical diffusion is enhanced when this "filter" is introduced. An analysis of this should be included in the "numerical von Neuman analysis" mentioned under General comments.*

The impact of this smoother is included in the sections with test analysis, plus two dedicated sections discuss it now. Please see above.

*Sect. 6.2 . It is really good that all these tests have been run. I don't think, however, that the weaknesses of the scheme are commented/recognised in sufficient depth. You should discuss the rather widespread noise away from the advected entities. The most depressing result is probably the tendency for the scheme to unmix even when the smoother is on (Figure 11). A general discussion of the Figures 7 through 11 should be included, which directly compare the results with some of the schemes in L14.*

The discussion has been strongly expanded in section 7.2 and the issues of the noise far from the advected bodies and the “unmix” included. We added new chart showing the mixing diagnostic, in addition to previously available numerical information printed on the “bow” charts. The corresponding discussion is added. We also highlighted that origin of some of the issues, first of all, the non-monotonic background, is not the scheme per-se (the 1D algorithm) but rather the dimensional split used for its implementation in 3D (well, 2D in that specific case). Similarly, the tendency to unmix the initially homogeneous field is due to this very splitting: the 1D algorithm transports a flat plain perfectly.

We also added the discussion on the smoother, which improves the linearity but: (i) it has low power against the background fluctuations, largely responsible for the unmix, (ii) we limited its power ( $\epsilon=0.08!$ ) in order to avoid excessive diffusivity. Therefore, remnants of the unmix still remained visible. We made it clear in the revised paper.

*l. 476 "Eq. (21)" should be "in Eq. (21)". However, I am a little confused since this equation relates to the vertical direction, while the tests described here are horizontal. I suspect that the equation number should be (20) and not (21). The correlated tracer runs are run both with and without the smoothing. It is unclear, however, if the smoother in (20) was applied to all other runs or if it has been included or not on an ad hoc basis. This must be clarified.*

We checked the numbering (of course, eq. 20, not 21) and made it clear throughout the paper what pictures represent the runs with / without the smoother.

*l. 506-514 It makes little sense to compare the performance of the Galperin scheme on one computer with that of other transport schemes, which are run on a different computer. One should instead compare directly with the performance of another transport scheme on the same computer. I suggest a simple (non-conserving) semi-Lagrangian scheme with bi-cubic interpolation. For a model like SILAM it is highly relevant to test the multi-tracer efficiency, as it was done for instance in Kaas et al. (2013), which you refer to. This should be done.*

We have reviewed the efficiency section, moved it to Discussion (now it is section 7.4) and provided more extensive analysis. In particular, it now includes the comparison with Bott scheme in its standard implementation available from internet – and with a simple semi-Lagrangian scheme made by ourselves. We also made a new subsection with analysis of the model scalability with regard to the number of species, horizontal resolution, and time step.

Regarding the comparison with HEL and CSLAM, in our experience the difference between the modern computers is usually comparatively small (tens of %) and Linpack benchmarks give a good representation of it for the purposes of dispersion modelling. The impact of implementation quality, however, can be large – e.g. we got a factor of 2-3 by quite basic optimization of our code for the Galperin scheme. We found Linpack scores for the processor used by Kaas et al – 20GFlops (now included in the paper, sorry for the omission), – similar to 18GFlops of our notebook. We also found another comparison of these CPUs with a different series of tests, which confirmed the similarity within some 20% margin. Therefore, the similarity between the machines is confirmed, with probably weaker computer used in our tests: Linpack is marginally lower and the bus capacity is quite low (a usual feature of notebooks). Therefore, we think that our comparison is fair: tests are identical, computers are similar and, most importantly, the implementations of the schemes come from their authors, i.e. their quality is as high as one can get. Together with comparison with “reference” implementation of Bott algorithm and the semi-Lagrangian scheme, this should give sufficient credibility to the efficiency assessment of the scheme. These issues are now explained in the paper.

# 1 Construction of the Eulerian atmospheric dispersion model

## 2 SILAM based on the advection algorithm of M.Galperin

3

4 M.Sofiev<sup>1</sup>, J.Vira<sup>1</sup>, R.Kouznetsov<sup>1,2</sup>, M.Prank<sup>1</sup>, J.Soares<sup>1</sup>, E.Genikhovich<sup>3</sup>

5 <sup>1</sup> Finnish Meteorological Institute, Helsinki, Finland

6 <sup>2</sup> A.M. Obukhov Institute for atmospheric Physics, Moscow, Russia

7 <sup>3</sup> Main Geophysical Observatory, St.Petersburg, Russia

8

### 9 1. Abstract

10 The paper presents the transport module of the System for Integrated modeLling of  
11 Atmospheric coMposition SILAM v.5 based on the advection algorithm of Michael Galperin.  
12 This advection routine, so far weakly presented in international literature, is positively  
13 defined, stable at any Courant number, and efficient computationally. We present the rigorous  
14 description of its original version, along with several updates that improve its monotonicity  
15 and shape preservation, allowing for applications to long-living species in conditions of  
16 complex atmospheric flows. The scheme is connected with other parts of the model in a way  
17 that preserves the sub-grid mass distribution information that is a corner-stone of the  
18 advection algorithm. The other parts include the previously developed vertical diffusion  
19 algorithm combined with dry deposition, a meteorological pre-processor, and chemical  
20 transformation modules.  
21 Quality of the advection routine is evaluated using a large set of tests. The original approach  
22 has been previously compared with several classic algorithms widely used in operational

23 dispersion models. The basic tests were repeated for the updated scheme and extended with  
24 real-wind simulations and demanding global 2-D tests recently suggested in literature, which  
25 allowed positioning the scheme with regard to sophisticated state-of-the-art approaches. The  
26 advection scheme performance was fully comparable with other algorithms, with a modest  
27 computational cost.

28 This work was the last project of Dr. Sci. Michael Galperin who untimely passed away on 17  
29 March 2008.

30

31 Keywords. advection schemes, numerical algorithms, dispersion modelling, Eulerian model.

32

33

## 34 **2. Introduction**

35 One of the key problems in atmospheric composition modelling is the accuracy and reliability  
36 of numerical schemes. A less appreciated but important issue is the consistency of the  
37 approaches applied in different modules of the modelling system. Usually, model construction  
38 follows process-wise split (Yanenko 1971; Marchuk 1995; Seinfeld & Pandis 2006), thus  
39 considering separately the advection and diffusion algorithms, physical and chemical  
40 transformations, and dry and wet deposition. In practical model developments, features of the  
41 transport algorithms, first of all, advection scheme, largely shape-up the model and determine  
42 its area of application.

### 43 **2.1. Advection schemes**

44 There are numerous types of advection schemes currently employed in atmospheric dispersion  
45 models. Two major categories refer to Lagrangian or Eulerian treatment of tracers: as small-

46 size masses (Lagrangian particles) or as the concentration fields discretised in a prescribed  
47 grid. The Eulerian schemes, the primary subject of this paper, can be divided to flux-form  
48 finite volume, semi-Lagrangian, or expansion-function schemes. The expansion-function  
49 schemes approximate the solution with a given set of basis functions and, in turn, can be  
50 divided to spectral, pseudospectral and finite-element approaches. Some classic schemes are  
51 also based on finite-difference approximations of the advective term of the transport equation.  
52 The basic principles of all these approaches were formulated several decades ago and, with  
53 certain modifications, are still in use. Many modern schemes combine several approaches.  
54 The large diversity of the advection algorithms is explained by a long list of requirements to  
55 such schemes. The most important ones are: positive definition, minimal numerical diffusion,  
56 limited non-monotonicity and non-linearity, stability with regard to high Courant number (the  
57 number of the model grid cells passed within one advection time step), small phase error,  
58 local and global mass conservation, and high numerical efficiency. Some of these  
59 requirements contradict to each other. For example, numerical diffusion “blurs” the resulting  
60 patterns but also makes them smoother, thus improving the monotonicity.

61 The finite-difference schemes involve direct discretization of the dispersion equation and  
62 various interpolation functions to evaluate derivatives of the concentration fields (see reviews  
63 of (Richtmyer 1962; Leith 1965; Roach 1980), as well as section 3.1 in (Rood 1987); specific  
64 examples are, for instance, (Russell & Lerner 1981; Van Leer 1974; Van Leer 1977; Van Leer  
65 1979). These schemes, being once popular, usually suffer from large numerical diffusion and  
66 limited stability, which sets stringent limitations to the Courant number usually requiring it to  
67 be substantially less than one. Therefore, the interest has gradually shifted towards flux,  
68 finite-element, and semi-Lagrangian schemes.

69 The flux schemes represent the transport via mass fluxes at the grid cell borders, which are  
70 calculated from concentrations in the neighbouring cells and wind characteristics. They are

71 inherently mass conservative and have become popular in atmospheric chemistry transport  
72 models (Kukkonen et al. 2012). Probably the most widely used flux-type scheme is the one  
73 made by A. Bott (Bott 1989; Bott 1992; Bott 1993), especially if one would count the  
74 numerous Bott-type schemes (see examples in (Syrovok 1996; Syrovok & Galperin 1997;  
75 Syrovok & Galperin 2000; Walcek & Aleksic 1998; Walcek 2000; Yamartino 1993), which  
76 are based on the same principle but involve different approximation functions, monotonicity  
77 and normalization procedures, etc.

78 The semi-Lagrangian schemes have been among the most-widely used approaches for  
79 decades, with numerous algorithms using its basic concept [*Crowley, 1968; Egan and*  
80 *Mahoney, 1972; Pedersen and Prahm, 1974; Pepper and Long, 1978; Prather, 1986;*  
81 *Smolarkiewicz, 1982; Staniforth and Cote, 1991* and references therein], [*Lowe et al., 2003;*  
82 *Sofiev, 2000*], etc. In the forward form, these schemes consider the transport of mass starting  
83 from the grid mesh points (departure points) and calculate the masses at the grid points closest  
84 to the arrival point. Backward algorithms start from arrival grid points and find the grid points  
85 near the departure point. The schemes can be based on tracking either grid points or grid cells  
86 along their trajectories. The gridpoint-based schemes are not inherently mass-conserving,  
87 whereas the volume-based schemes achieve mass conservation by integrating the mass over  
88 the departure volume. They can sometimes be described as a combination of finite-volume  
89 and semi-Lagrangian methods (Lin & Rood 1996, 1997). Stability of these schemes can be  
90 ensured for a wide range of Courant numbers (Leonard 2002). A general review can be found  
91 in (Lauritzen et al. 2011), whereas a comparison of 19 modern schemes is discussed in  
92 (Lauritzen et al. 2014), hereinafter referred to as L14.

93 Modelling in spectral space is another approach with long history (Ritchie 1988; Kreiss &  
94 Olinger 1972; Zlatev & Berkowicz 1988; Prahm & Christensen 1977) but not widely used  
95 today.

**Deleted:** It is based on solving the transport equation in spectral space.

98 One of the main problems of the existing schemes is substantial numerical diffusion  
99 originating from the finite-step discretization along space and time. Seemingly inevitable in  
100 Eulerian context, this phenomenon, however, does not exist in Lagrangian advection schemes,  
101 which do not contain explicit discretization of particle movement. Lagrangian domain is a  
102 continuous space rather than a set of pre-defined grid meshes and the position of the particles  
103 can be calculated precisely. As a result, numerical diffusion of purely Lagrangian schemes is  
104 always zero – at a cost of strongly non-monotonous concentration fields due to limited spatial  
105 representativeness of a single Lagrangian particle and ~~a limited number of particles.~~

Deleted: the

106 One of ways to reduce the diffusivity of an Eulerian scheme is to store additional prognostic  
107 variables to describe the state of each grid cell with higher spatial resolution than the formal  
108 cell size: a sub-grid mass distribution. This can take a form of extra conservation equation(s)  
109 for, e.g., first- or higher-order moments (Egan & Mahoney 1972; Prather 1986). There are  
110 other approaches that use different kind of the extra information. For instance, the  
111 Conservative Semi-Lagrangian schemes (Yabe & Aoki 1991; Yabe et al. 2001) use a semi-  
112 Lagrangian step to evaluate the mixing ratio at cell interfaces, and then use the interface  
113 values along with the cell integrals to derive an interpolant representing the sub-grid  
114 distribution.

Deleted: It allows to add

Deleted: , thus preserving more features of the concentration field

115 In a series of works, Michael Galperin developed a semi-Lagrangian scheme that used the  
116 sub-grid information on mass centre location inside the cell. The scheme was made fully non-  
117 diffusive for isolated plumes, positively defined, and very efficient computationally (Galperin  
118 et al. 1994; Galperin et al. 1995; Galperin et al. 1997; Galperin 1999; Galperin & Sofiev  
119 1998; Galperin & Sofiev 1995; Galperin 2000). The early version of this scheme applied in  
120 the large-scale modelling by (Sofiev 2000) resembled the “moving-centre” approach widely  
121 used in aerosol dynamics models (Kokkola et al. 2008) and shared its characteristic weakness  
122 – high non-monotonicity. The later developments substantially reduced it without damaging

127 other features (Galperin 1999; Galperin 2000). Further development of this scheme is the  
128 subject of the current paper.

## 129 **2.2. Horizontal and vertical diffusion, dry deposition**

130 Diffusion algorithms are less diverse than advection schemes. The physical ground for one of  
131 the common diffusion parameterizations is described in details by (Smagorinsky 1963), who  
132 suggested a formula for grid-scale scalar eddy-diffusivity based on the model resolution and  
133 wind speed derivatives, thus connecting the numerical features of the simulations and  
134 hydrodynamics. It is widely used in chemical transport models (Kukkonen et al. 2012).

135 The dry deposition is usually accounted for as a boundary condition to the vertical advection-  
136 diffusion equation. Computation of dry deposition for gases practically always follows the  
137 electrical analogy, for which one of the first comprehensive parameterizations was suggested  
138 by (Wesely 1989). Among the extensions of this approach, one was suggested by Sofiev,  
139 (2002), who combined it with vertical diffusion and connected with the Galperin advection  
140 scheme. The algorithm used effective mean diffusion coefficient over thick layers calculated  
141 from high-resolution meteorological vertical profiles, the direction also recommended by  
142 Venkatram & Pleim (1999). These thick layers were ~~terminated~~ using the subgrid information  
143 available from the advection scheme, which increased the accuracy of both algorithms (Sofiev  
144 2002).

Deleted: fined

145 For aerosol species, the electrical analogy is not correct (Venkatram & Pleim 1999).

146 Compromising approaches suggested by (Slinn 1982; Zhang et al. 2001) and updated by  
147 Petroff and Zhang (2010) involve numerous empirical relations, sometimes ~~on~~ thin ground.

Deleted: with

148 More rigorous approach unifying the gas and aerosol deposition parameterizations into a  
149 single solution was developed by (Kouznetsov & Sofiev 2012).

## 152 **2.3. Organization of the paper**

153 The current paper describes the Eulerian transport algorithm of the System for Integrated  
154 modeLling of Atmospheric coMposition SILAM v.5, which is based on the advection scheme  
155 of Michael Galperin with several updates.

156 The paper is organised as follows. Section 3 describes the original algorithm of M. Galperin  
157 and positions the scheme among other approaches. Section 4 presents the improvements made  
158 during its implementation and testing in SILAM. The Section 5 outlines the scheme  
159 interconnections with other model parts. Standard and advanced model tests are shown in  
160 section 6. Finally, discussion in the section 7 includes analysis of the scheme performance in  
161 the tests, as well as comparison with other algorithms.

162 Following the SILAM standards, all units throughout the paper are the basic SI: [mole] for  
163 chemicals, [kg] for aerosols without chemical speciation, [m] for distance and size, [sec] for  
164 time, etc. The model operates with concentrations, [mol m<sup>-3</sup>] or [kg m<sup>-3</sup>]. Some of the below  
165 tests are formulated in mixing ratios [mol mol<sup>-1</sup>] or [kg kg<sup>-1</sup>].

166

## 167 **3. Background**

### 168 **3.1. Basic equations**

169 We consider the forward dispersion equation with the first-order K-theory-based closure for  
170 diffusion:

171 (1) 
$$L\varphi = E, \quad \text{where } L = \frac{\partial}{\partial t} + \frac{\partial}{\partial \xi_i} (u_i) - \frac{\partial}{\partial \xi_i} \rho \mu_{ij} \frac{\partial}{\partial \xi_j} \frac{1}{\rho} + \zeta.$$

172 Here  $\varphi$  is concentration of the pollutant,  $t$  is time,  $E$  is emission term,  $\xi_i$ ,  $i = 1..3$  denote the  
173 three spatial axes,  $u_i$  are components of the transport velocity vector along these axes,  $\mu_{ij}$  are

174 components of the turbulent diffusivity tensor,  $\rho$  is air density, and  $\zeta$  represents  
175 transformation source and sink processes.

176 Equation (1) is considered on the time interval  $t \in (t_0, t_N)$  in the domain  
177  $\{\xi_i\} \in \Xi = [h_l, H] \times \Omega$ , where the heights  $h_l$  and  $H$  are the lower and upper boundaries of the  
178 computational domain and  $\Omega$  is the horizontal computational area with border  $\partial\Omega$ . The initial  
179 conditions are:

180 (2) 
$$\varphi|_{t=t_0} = \varphi_0(\vec{\xi})$$

181 Boundary conditions depend on type of the simulations. In a general form, they constrain  
182 concentration and/or its first derivative:

183 (3) 
$$\alpha \frac{\partial \varphi}{\partial \xi_i} \Big|_{\xi_j \in \partial \Xi} + \beta \varphi|_{\xi_j \in \partial \Xi} = \gamma$$

184 Here the values of  $\alpha$ ,  $\beta$ , and  $\gamma$  depend on type of the boundary. In particular, dry deposition at  
185 the surface  $\xi_3 = h_l$  is described via  $\alpha = \mu_{33}$ ,  $\beta = -v_d$  (dry deposition velocity),  $\gamma = 0$ ; prescribed  
186 concentration  $\varphi_l$  at the lateral boundaries  $\xi_{1,2} \in \partial\Omega$  implies  $\alpha = 0$ ,  $\beta = 1$ ,  $\gamma = \varphi_l$ , etc. A global  
187 domain would require periodic longitudinal conditions.

### 188 3.2. Advection scheme of Michael Galperin

189 The current section presents the advection algorithm suggested by Michael Galperin in 2000s  
190 as a contribution to Eulerian transport scheme of SILAM. The idea of the scheme can be  
191 found in a short methodological publication of (Galperin 2000) (in Russian) and conference  
192 materials (Galperin 1999; Sofiev et al. 2008). It is very briefly outlined by (Petrova et al.  
193 2008) (hereinafter referred to as P08) but no systematic description exists so far.

Deleted: (1

Deleted: dynamics

196 For the 1-D case, let us define the simulation grid,  $\xi_I = x$ , as a set of  $I$  grid cells  $i = 1..I$ . Let the  
 197 coordinate of the centre of the  $i$ -th grid cell be  $x_i$ , and coordinates of the cell left- and right-  
 198 hand borders be  $x_{i-0.5}$  and  $x_{i+0.5}$ , respectively. The 1-D cell size is then  $V_i = x_{i+0.5} - x_{i-0.5}$ . The  
 199 advected field  $\varphi$ , in each grid cell  $i$ , is defined via the total mass in the cell  $M_i$  and position of  
 200 the centre of mass  $X_i$ ,  $X_i \in [x_{i-0.5}, x_{i+0.5}]$ :

$$\begin{aligned}
 (4) \quad M_i &= \int_{x_{i-0.5}}^{x_{i+0.5}} \varphi(x) dx \\
 X_i &= \frac{1}{M_i} \int_{x_{i-0.5}}^{x_{i+0.5}} x \varphi(x) dx
 \end{aligned}$$

202 Let us represent the mass distribution in each grid cell via the rectangular slab:

$$(5) \quad \pi_i^n(x) = \begin{cases} \frac{1}{2\omega_i^n}, & |x - X_i^n| \leq \omega_i^n \\ 0, & \text{otherwise} \end{cases},$$

204 where  $n$  is time step and  $\omega_i^n = \min(|X_i^n - x_{i-0.5}|, |X_i^n - x_{i+0.5}|)$  is distance from the centre of  
 205 mass  $X_i^n$  to the nearest border of the cell  $i$ . Eq. (5) defines the widest unit-volume slab that  
 206 can be confined inside the cell (Figure 1) for the given centre of mass.

207 The advection scheme consists of a transport step and a reprojection step. At the transport  
 208 step, each slab  $\pi_i$  is moved along the velocity field  $u(x)$ . Advection of the slab does not  
 209 change its shape within the time step  $\delta t = t_{n+1} - t_n$  but can move it anywhere over the domain  
 210 or bring outside. In essence, the slab transport is replaced with advection of its mass centre,  
 211 which during this time step becomes analogous to a Lagrangian particle:

$$(6) \quad X_i^{n+1} = X_i^n + \int_{t_n}^{t_{n+1}} u(X_i^n, t) dt,$$

Deleted: The

Deleted: (5

Deleted: -

216 where  $u(X_i^n, t)$  is wind speed at the mass centre location.

217 The original Galperin scheme employed wind at the cell mid-point  $x_i$  and used explicit first-  
218 order time discretization:  $u(x_i^n, t_n) = u_i^n$ . Then the transported slab is given by:

219 (7) 
$$\tilde{\pi}_i^n(x) = \pi_i^n(x - u_i^n \delta t)$$

220 Following the transport step (7), the masses  $M_k$  and centres of mass  $X_k$  of the receiving set  
221 of cells  $k \in K$  are updated using the transported slabs  $\tilde{\pi}_i^n$ :

222 (8) 
$$M_k^{n+1} = \sum_{i=1}^{N_k} \alpha_{i,k} M_i^n$$
$$X_k^{n+1} = \frac{1}{M_k^{n+1}} \sum_{i=1}^{N_k} \beta_{i,k} M_i^n,$$

223 where  $\alpha_{i,k} = \int_{x_k-0.5}^{x_k+0.5} \tilde{\pi}_i^n(x) dx$  and  $\beta_{i,k} = \int_{x_k-0.5}^{x_k+0.5} x \tilde{\pi}_i^n(x) dx$  correspond to the mass and the first  
224 moment fractions arriving from the cell  $i$  into cell  $k$ . The integrals are easy to evaluate due to  
225 the simple form of  $\pi_i^n(x)$  in Eq. (5). In-essence, Eq. (8) describes a mass-conservative  
226 projection of the advected slab to the computation grid.

227 The coefficients  $\alpha_{i,0} = \int_{-\infty}^{0.5} \tilde{\pi}_i^n(x) dx$  and  $\alpha_{i,I+1} = \int_{I+0.5}^{\infty} \tilde{\pi}_i^n(x) dx$  determine the transport outside  
228 the domain through the left and right borders, respectively, i.e. the scheme is fully  
229 accountable and mass-conservative since  $\sum_k \alpha_{i,k} = \int_{-\infty}^{\infty} \tilde{\pi}_i^n(x) dx = 1$  for each  $i$ . Also, since the  
230 functions  $\pi_i^n(x)$  are nonnegative, the coefficients  $\alpha_{i,k}$  are nonnegative, and consequently  
231  $M_k^{n+1} \geq 0$  as long as  $M_i^n \geq 0$  for all  $i$ . It means that the scheme is positively defined for any  
232 simulation setup:  $u$ ,  $\Delta t$ , and discretization grid.

Deleted: the

Deleted: (5)

235 In multiple dimensions, the slabs are described by the total mass in multidimensional cell and  
 236 centres of mass along each dimension. In two dimensions, an analogue of Eq. (5) will be.

Deleted: (5)

237 (9) 
$$\Pi_{i,j}^n(x, y) = \pi_{i,j}^n(x) \pi_{i,j}^n(y)$$

238 where the functions  $\pi_{i,j}(x)$  and  $\pi_{i,j}(y)$  depend on  $X_{i,j}$  and  $Y_{i,j}$ , respectively. The advection  
 239 step in form of (7) and the slab projection integrals (8) are then defined in 2D space.

240 However, a simpler procedure used in the original scheme is obtained with dimensional  
 241 splitting, where the transport in each dimension is processed sequentially with the grid  
 242 projection applied in-between. For an x-y split, the intermediate distribution for each row  $j$  is  
 243 obtained by setting:

244 (10) 
$$\Pi_{i,j}^{n+1/2}(x, y) = \tilde{\pi}_{i,j}^n(x) \pi_{i,j}^n(y),$$

245 evaluating  $\alpha_{i,k}$  and  $\beta_{i,k}$  from  $\tilde{\pi}_{i,j}^n(x)$  and updating  $M_{i,j}$ ,  $X_{i,j}$  and  $Y_{i,j}$ . Since

246 
$$\int_{y_j-0.5}^{y_j+0.5} \pi_{i,j}(y) dy = 1 \text{ and } \int_{y_j-0.5}^{y_j+0.5} y \pi_{i,j}(y) dy = Y_{i,j}^n,$$
 the two-dimensional slab projection simplifies

247 to:

248 (11) 
$$\begin{aligned} M_{k,j}^{n+1/2} &= \sum_{i=1}^{N_x} \alpha_{i,k} M_{i,j}^n \\ X_{k,j}^{n+1/2} &= \frac{1}{M_k^{n+1/2}} \sum_{i=1}^{N_x} \beta_{i,k} M_{i,j}^n \\ Y_{k,j}^{n+1/2} &= \frac{1}{M_k^{n+1/2}} \sum_{i=1}^{N_x} \alpha_{i,k} M_{i,j}^n Y_{i,j}^n. \end{aligned}$$

249 The y-advection is then performed by taking the transport step for  $\pi_{i,j}^{n+1/2}(y)$  starting from

250  $Y_i^{n+1/2}$ , evaluating  $\alpha_{i,k}$  and  $\beta_{i,k}$  from  $\tilde{\pi}_{i,j}^{n+1/2}(y)$ , and applying the reprojection (11) with  $X$

251 and  $Y$  inverted. The generalisation to three dimensions is analogous.

### 253 **3.3. Relations of Galperin scheme to other approaches**

254 The Galperin scheme shares some features with other approaches (see reviews (Rood 1987)  
255 and (Lauritzen et al. 2011)). Arguably the closest existing scheme is the finite-volume  
256 approach of (Egan & Mahoney 1972), hereinafter referred to as EM72, and (Prather 1986),  
257 hereinafter P86. The main similarity between these schemes is the representation of the mass  
258 distribution via a set of slabs (rectangular in EM72 and continuous polynomial distributions in  
259 P86), one per grid cell, with the mass centre identified via the slab first moment, plus  
260 additional constraints. During the EM72 and P86 advection step, mass and the first moment  
261 are conserved, similarly to the reprojection step (8). However, this expires the similarity.  
262 There are several principal differences between the EM72/P86 and Galperin algorithms.  
263 Firstly, in EM72 the slab width is computed via the second moment (variance) of the mass  
264 distribution in the grid cell. P86 uses the second moments to constrain the shape of the  
265 polynomials. As a result, this moment has to be computed and stored for the whole grid, and  
266 the corresponding conservation equation has to be added, on top of those for the mass and the  
267 first moment. The Galperin's approach does not require the second moment, instead  
268 positioning the slab against the cell wall. In fact, EM72 pointed out that the second moment  
269 can be omitted but did not use the wall-based constrain in such "degenerated" scheme, which  
270 severely affected its accuracy.  
271 Secondly, EM72 uses the movements of the slabs in adjacent grid cells to calculate the mass  
272 flows across the border. Such local consideration requires the Courant number to be less than  
273 1: the so-called "portioning parameter" (a close analogy to the Courant number in the scheme)  
274 is limited between 0 and 1. The same limitation is valid for P86 approach. Galperin's scheme  
275 can be applied at any Courant number and its reprojection step can rather be related to (Lin &  
276 Rood 1996).

277

## 278 4. Updates of the scheme in SILAM v.5

279 There are several features of the original scheme, which make it difficult to use in large-scale  
280 chemical transport simulations. These are listed here and the corresponding improvements are  
281 introduced in the following sub-sections.

- 282 - The scheme is formulated with zero inflow boundary conditions
- 283 - Real-wind tests have shown that the scheme has difficulties in complex-wind and  
284 complex-terrain conditions, similar to EM72 (Ghods et al. 2000)
- 285 - The explicit forward-in-time advection ( 7) is inaccurate
- 286 - The scheme, being very good with individual sharp plumes over zero background,  
287 noticeably distorts the smoother fields with non-zero background – see P08.

288 In addition, the accuracy of the dimension split was increased via symmetrisation: the order of  
289 dimensions in SILAM routines is inverted each time step: x-y-z-z-y-x (Marchuk 1995).

Moved (insertion)[1]

Deleted: T

Deleted: ¶

### 290 4.1. Lateral and top boundary conditions

291 The open boundary for the outgoing masses is kept in SILAM regional simulations. The  
292 inflow into a limited-area domain is defined via prescribed concentration at the boundary ( 3),  
293  $\alpha=0, \beta=1, \gamma=\varphi_l$ . The mass coming into the domain during a single time step is equal to:

$$294 \quad (12) \quad \begin{aligned} M_1^{in} &= \varphi_l(x_{0.5}) u(x_{0.5}) \mathcal{N}(u(x_{0.5})) \delta t \\ M_l^{in} &= \varphi_l(x_{l+0.5}) |u(x_{l+0.5})| \mathcal{N}(-u(x_{l+0.5})) \delta t \end{aligned}$$

295 Here  $\mathcal{N}(u)$  is Heaviside function ( $= 1$  if  $u > 0$ ,  $= 0$  if  $u \leq 0$ ). Assuming the locally-constant  
296 wind we obtain that  $M^{in}$  is distributed uniformly inside the slab similar to that of ( 5). For,  
297 e.g., the left-hand-border, the continuous form will read:

Deleted: ( 5)

$$298 \quad (13) \quad \Pi_m^{n+1}(x) = \begin{cases} \varphi_l(x_{0.5}) \mathcal{N}(u(x_{0.5}, t_k)) \delta t, & x \in [x_{0.5}, x_{0.5} + u(x_{0.5}, t_n) \mathcal{N}(u(x_{0.5}, t_n)) \delta t] \\ 0, & otherwise \end{cases}$$

302 It is then projected to the calculation grid following ( 8).

303 The top boundary follows the same rules as the lateral boundaries. At the surface, the vertical  
304 wind component is zero, which is equivalent to closure of the domain with regard to  
305 advection.

306 Global-domain calculations require certain care: SILAM operates in longitude - latitude grids,  
307 i.e. it has singularity points at the poles and a cut along the 180E line. For longitude, if a  
308 position of a slab part appears to be west of -180E or east of 180E, it is increased or decreased  
309 by 360 degrees, respectively. Resolving the pole singularity is done via reserving a cylindrical  
310 reservoir over each pole. The radius of the reservoirs depends on the calculation grid  
311 resolution but is kept close to 2 degrees. The calculation grid reaches the borders of the  
312 reservoirs, whose mean concentrations are used for the lateral boundary conditions:

$$(14) \quad \begin{aligned} \varphi \Big|_{y_2=y_{2-0.5}} &= \varphi_{S\_pole}(t, z) \\ \varphi \Big|_{y_2=y_{2-J+0.5}} &= \varphi_{N\_pole}(t, z) \end{aligned}$$

314 Vertical motion in the pole cylinders is calculated separately using vertical wind component  
315 diagnosed from global non-divergence requirement.

#### 316 **4.2. Extension of the scheme for complex wind pattern**

317 The original Galperin scheme tends to accumulate mass at stagnation points where one of the  
318 wind components is small. Similar problems were reported by (Ghods et al. 2000) for the  
319 EM72. Ghods et al. (2000) also suggested an explanation and a generic principle for solving  
320 the problem: increasing the number of points at which the wind is evaluated inside the grid  
321 cell. For application in the Galperin scheme, it can be achieved by separate advection of each  
322 slab edge instead of advecting the slab as a whole. This allows for shrinking and stretching  
323 the slab following the gradient of the velocity field. Formally, this can be written as follows.

Deleted: In

Deleted: to

326 Let's again consider the 1-D slab that has been formed according to (5). Its edges are:

Deleted: ( 5

327 (15) 
$$X_{L,i} = X_i - \omega_i, \quad X_{R,i} = X_i + \omega_i$$

328 The advection step takes the wind velocity at the left and right slab edges and transports them

329 in a way similar to (6) with the corresponding wind velocities. The new slab is formed as a

Deleted: ( 6

330 uniform distribution between the new positions of the edges:

331 (16) 
$$\tilde{\pi}_i^{k+1}(x) = \begin{cases} \frac{1}{\tilde{X}_{R,i}^k - \tilde{X}_{L,i}^k}, & \tilde{X}_{L,i}^{k+1} \leq x \leq \tilde{X}_{R,i}^{k+1} \\ 0, & \text{otherwise} \end{cases},$$

332 Where  $\tilde{X}_{L,i}^k, \tilde{X}_{R,i}^k$  are the new positions of the slab edges at the end of the time step. This new-

333 slab is then projected following Eq. (8).

334

Moved up [1]: The accuracy of the dimension split was increased via symmetrisation: the order of dimensions in SILAM routines is inverted each time step: x-y-z-z-y-x (Marchuk 1995).¶

### 335 4.3. Changing wind along the mass-centre trajectory

336 The explicit advection step (7) is inaccurate and can be improved under assumption of linear

337 change of wind inside each grid cell, with values at the borders coming from the meteo input:

338 (17) 
$$u(x) = u(x_{i-0.5}, t_n) \frac{(x_{i+0.5} - x)}{(x_{i+0.5} - x_{i-0.5})} + u(x_{i+0.5}, t_n) \frac{(x - x_{i-0.5})}{(x_{i+0.5} - x_{i-0.5})}, \quad x_{i-0.5} \leq x \leq x_{i+0.5}$$

339 Then, the trajectory equation (6) can be piece-wise integrated analytically for each slab edge.

Deleted: ( 6

340 Let's denote  $\Delta u = u_{i+0.5} - u_{i-0.5}$ ,  $\Delta t = t_{n+1} - t_n$ ,  $\alpha = \Delta u / \Delta t$  and consider the transport starting

341 at, e.g.  $x_{i-0.5}$ . Then the time needed for passing through the entire cell,  $\Delta x = x_{i+0.5} - x_{i-0.5}$  is:

342 (18) 
$$T_{cell} = \log(1 + \alpha \Delta x u_i) / \alpha$$

343 If  $\Delta t < T_{cell}$ , the point will not pass through the whole cell and stop at:

344 (19) 
$$x_{\Delta t} = x_{i-0.5} + u_i (\exp \alpha t - 1) / \alpha$$

353 Applying sequentially ( 18) and ( 19) until completing the model time step  $\Delta t$  , one obtains  
 354 the analytical solution for the final position of the slab edges.  
 355 This approach neglects the change of wind with time. However, the integration method is  
 356 robust, since the linearly interpolated wind field is Lipschitz-continuous everywhere, which in  
 357 turn guarantees the uniqueness of the trajectories of  $X_L$  and  $X_R$  . Therefore, using the  
 358 analytic solution ( 18) and ( 19), the borders of the slabs will never cross.

#### 359 **4.4. Reducing the shape distortions**

360 The original scheme tends to artificially sharpen the plume edges and to gradually redistribute  
 361 the background mass in the vicinity of the plume towards it (Figure 2, blue shapes). Similar  
 362 “antidiffusive” distortions were also reported by P08 and by EM72 – for their scheme.

363 The reason for the feature can be seen from Eq. ( 8): if a large mass is concentrated at one of  
 364 the grid cell sides, the centre of mass becomes insensitive to the low -mass part of the cell, i.e.  
 365 a small mass that appears there from the neighbouring cell is just added to the big slab with  
 366 little effect on its position and width.

367 A cheap, albeit not rigorous, way to confront the effect is to compensate it via additional  
 368 small pull of the mass centre towards the cell midpoint before forming the slab for advection:

369 ( 20) 
$$\hat{X}_i^n = x_i + (X_i^n - x_i)(1 - \varepsilon),$$

370 where  $\varepsilon$  is smoothing factor. The adjusted mass centre  $\hat{X}_i^n$  is then used to form the slab ( 5).

371 The way this smoother works gets clearer if one notices that the Galperin scheme becomes  
 372 similar to the upwind algorithm if the locations of the centres of masses are always forced to  
 373 the middle of the grid cells at the beginning of time step. The upwind scheme is very  
 374 diffusive, and relaxation towards it confronts the anti-diffusive features of the Galperin  
 375 approach. Actual value of  $\varepsilon$  cannot be easily obtained from some optimization problem. Its

Deleted: D  
 Deleted: of the same origin  
 Deleted: for Galperin's approach

Deleted: ~0.08  
 Deleted: an empirically found  
 Deleted: correction  
 Deleted: ( 5

383 increase from 0 up to 1 gradually makes the scheme more and more diffusive, with the above  
384 distortions becoming negligible by  $\varepsilon \sim 0.08$  (Figure 2, red shapes). This behaviour and the  
385 value were similar for various Courant numbers and tests. It is also seen from the spectral  
386 features of the scheme in the next section – and further discussed in relation to scheme tests.

#### 387 **4.5. Analysis in frequency space**

388 The non-linearity introduced by the coupling of cell mass and centre of mass in Eq. ( 8)  
389 makes formal stability and convergence analysis after Charney et al., (1950) difficult.  
390 However, the features of the scheme can be investigated numerically following the approach  
391 of Kaas & Nielsen, (2010).

392 The scheme was run for 200 time steps in a 1D domain with 100 grid points. For each  
393 wavenumber up to 25, the scheme was initialized with the corresponding sine function, and  
394 run with Courant numbers ranging from 0.05 to 0.95 in steps of 0.05. This allowed evaluating  
395 the spectrally resolved root mean squared error (RMSE) and, after a Fourier transform, the  
396 spectral amplification factor (cumulative for the 200 steps) for each wavenumber. The  
397 amplification factor quantifies the scheme's ability to resolve the corresponding harmonics,  
398 while the RMSE additionally includes the effect of phase errors and possible spurious modes.  
399 Since the scheme is formulated for nonnegative concentrations, a constant background  $B = 1$   
400 is added to each waveform.

401 Figure 3 presents the amplification factor and RMSE for the Galperin scheme without the  
402 smoother (panels a,d) and with it,  $\varepsilon = 0.08$  (panels c,f). Furthermore, the impact of doubling  
403 the background component to twice the wave amplitude is shown (panels b,e). In the case of  
404  $B = 1$ , the scheme without smoother shows only minor damping of all considered  
405 wavenumbers ( $k$  up to 25). The RMSE has a maximum for  $k$  between 5 and 10 but stays  
406 almost constant from  $k = 10$  to  $k = 25$ . This shows the scheme's ability to resolve sharp

Formatted: Heading 2

Deleted: (

408 gradients when there is no significant background. The cumulative amplifying factors for  
409 some wavelengths exceed one but this does not imply instability since the single-step  
410 amplifying factors fluctuate depending on the positions of centres of mass. If the integration is  
411 continued over large number of timesteps (not shown), the solution converges to a  
412 combination of rectangular pulses (a similar feature was mentioned in EM72 for that scheme).  
413 Introducing the smoothing  $\varepsilon = 0.08$  resulted in strong attenuation of high-frequency  
414 components and increased the RMSE for wavenumbers above  $\sim 10$ . Since the smoothing  
415 factor effectively damps the fluctuations of the centres of mass, the amplification factors are  
416 below one for all wavenumbers. Adding a background term also reduces the responsiveness  
417 of the mass centres to newly coming amounts (see Eq ( 8)), which leads to a similar damping  
418 of the higher frequencies in Figure 3c, f.

Formatted: Font: Italic

419 To further investigate the spectral response of the scheme, it was evaluated with a broadband  
420 input:

421 ( 21)  $f(x) = \sin(2\pi x \cos(20\pi x)) + B$ .

422 Figure 4, left panel, depicts the power spectral densities for the exact and numerical solutions  
423 after a single revolution with CF=0.7 and 100 grid points. The corresponding solutions are  
424 shown in the right panel. For the comparison, results are also shown for the 4th order Bott  
425 (1989) scheme without shape preservation, and for a generic non-conservative upstream semi-  
426 Lagrangian scheme with cubic spline interpolation.

427 With  $B = 1$ , all schemes capture the first spectral peaks around  $k = 10$  and therefore resolve  
428 most of the spectral content. Without smoother, the Galperin scheme follows the spectrum of  
429 the true solution also resolves the spectral features around  $k = 30$ . Application of the  
430 smoother leads to damping effect throughout the spectrum, including the spurious high-

431 frequency components, such as the peak at  $k = 40$ . This illustrates the use of the smoother for  
432 reducing over- and undershoots, as discussed in Section 4.4.  
433 Similarly to the single-harmonic tests, the situation changes in presence of a significant  
434 background ( $B = 2$ ). Regardless of smoothing, the Galperin scheme damps the spectral peaks  
435 starting around  $k = 10$ , which corresponds to the reduction of amplitude visible in the  
436 numerical solution.

437

## 438 **5. Connection of the advection scheme with other SILAM** 439 **modules**

440 Construction of the dispersion model using the Galperin advection scheme as its transport  
441 core is not trivial because all other modules should support the use of the sub-grid information  
442 on positions of the mass centres. In some cases it is straightforward but in others one can only  
443 make the module to return them undamaged back to advection.

### 444 **5.1. Vertical axis: combined advection, diffusion, and dry** 445 **deposition**

446 For the vertical axis, SILAM combines the Galperin advection with the vertical diffusion  
447 algorithm following the extended resistance analogy (Sofiev 2002), which considers air  
448 column as a sequence of thick layers. Vertical slabs within these layers are controlled by the  
449 same 1-D advection, which is performed in absolute coordinates – either z- or p- depending  
450 on the vertical (height above the surface or hybrid). Settling of particles is included into  
451 advection for all layers except for the first one, where the exchange with the surface is treated  
452 by the dry deposition scheme.

453 The centres of masses are used but not modified by diffusion: the effective diffusion  
454 coefficient between the neighbouring thick layers is taken as an inverse of aerodynamic  
455 resistance between the centres of mass of these layers (Sofiev 2002):

456 ( 22)

$$\langle K_{i,i+1} \rangle = \frac{\Delta z_{i,i+1}}{\int_{Z_i}^{Z_{i+1}} \frac{dz}{K_z(z)}}$$

Deleted: 21

457 The effective thickness  $\Delta z_{i,i+1}$  is taken proportional to pressure drop between the centres of  
458 masses, which assures equilibration of mixing ratios due to diffusion.

459 In the lowest layer, the dry deposition velocity is calculated at the height of centre of mass  $Z_l$   
460 following the approach of (Kouznetsov & Sofiev 2012).

461 The advantages of using the mass centres as the vertical diffusion meshes are discussed in  
462 details by (Sofiev 2002), where it is shown that the effect can be substantial if an inversion  
463 layer appears inside the thick dispersion layer. Then the location of the mass centre above /  
464 below the inversion can change the up / down diffusion fluxes by a factor of several times.

## 465 5.2. Emission-to-dispersion interface

466 Emission data is the only source of sub-grid information apart from the advection itself:

467 location of the sources is transformed into the mass centre positions of their emission.

468 For point sources, the mass is added to the corresponding grid cell and centres of masses are

469 updated:

470 ( 23)

$$\begin{aligned}\hat{M}_{ijk} &= M_{ijk} + M_{ems} \\ \hat{X}_{ijk} &= (X_{ijk} M_{ijk} + M_{ems} X_{ems}) / \hat{M}_{ijk} \\ \hat{Y}_{ijk} &= (Y_{ijk} M_{ijk} + M_{ems} Y_{ems}) / \hat{M}_{ijk} \\ \hat{Z}_{ijk}^k &= (Z_{ijk}^k M_{ijk} + M_{ems} Z_{ems}^k) / \hat{M}_{ijk}\end{aligned}$$

Deleted: 22

471 where  $M_{ems}$  is the mass emitted to the cell  $(i, j, k)$  during the time step,  $X_{ems}$ ,  $Y_{ems}$  are the

472 coordinates of the source in the grid and  $Z_{ems}^k$  is the effective injection height in the layer  $k$ ,

473 equal to middle of the layer if no particular information is available.

476 For area sources, the approach depends on the source grid. If it is the same as the  
 477 computational one, the mass centre is put to the middle of the cell (no extra information can  
 478 be obtained). If the grids are different, the source is reprojected. For each computational grid  
 479 cell  $(i, j)$ , the centre of mass of emission is:

480 ( 24) 
$$X_{em,ij} = \frac{\iint_{(x,y) \in (i,j)} xM(x,y) dx dy}{\iint_{(x,y) \in (i,j)} M(x,y) dx dy}; \quad Y_{em,ij} = \frac{\iint_{(x,y) \in (i,j)} yM(x,y) dx dy}{\iint_{(x,y) \in (i,j)} M(x,y) dx dy}$$

481 Where  $M(x, y)$  denotes the original source distribution. After that, the procedure is the same as  
 482 in the case of point source ( 23).

### 483 5.3. *Meteo-to-dispersion interface*

484 Modifications described in section 4 require staggered wind fields, which have to be provided  
 485 by the meteo pre-processor (unless they are directly available from the input data). Moreover,  
 486 the pre-processor needs to ensure consistency between the flow and air density fields (Prather  
 487 et al. 1987; Rotman et al. 2004; Robertson & Langner 1999). This is particularly important  
 488 with the present advection scheme, since mixing ratio perturbations caused by the mass-flow  
 489 inconsistency are not suppressed by numerical diffusion.

490 The wind pre-processing follows the idea of “pressure fixer”, which means adding a  
 491 correction  $\delta \mathbf{V}$  to the original horizontal wind field  $\mathbf{V}_0$  such that for their sum, the vertical  
 492 integral of mass flux divergence corresponds to the surface pressure tendency:

493 ( 25) 
$$\int_0^{p_s} \nabla \cdot (\mathbf{V}_0 + \delta \mathbf{V}) dp = -\frac{\partial p_s}{\partial t},$$

494 where the surface pressure tendency  $\partial p_s / \partial t$  is evaluated from the meteorological input data.

495 The correction  $\delta \mathbf{V}$  is not uniquely determined, and SILAM adopts the algorithm of Heimann

Deleted: 23

Deleted: ( 22

Deleted: 24

499 & Keeling (1989), where the correction term is given by the gradient of a two-dimensional  
500 potential function:

501 (26) 
$$\delta \mathbf{V} = \nabla \psi(x, y).$$

Deleted: 25

502 Substituting (26) into (25) yields a Poisson equation for  $\psi(x, y)$ , which is solved to  
503 subsequently recover  $\delta \mathbf{V}$ . The obtained correction flux is then distributed within the column  
504 proportionally to the air mass in each layer, ending up with the corrections to the horizontal  
505 winds. The vertical wind is then evaluated in each column to enforce the proper air mass  
506 change in each cell.

Deleted: (25

Deleted: (24

#### 507 **5.4. Chemical module interface**

508 This interface is implemented in a very simple manner: the mass centres are not affected by  
509 the transformations. Chemical module deals exclusively with concentrations in the grid cells.  
510 The newly created mass is added to the existing one, thus accepting its centre position in the  
511 cell. If some species did not exist before the transformation the new mass centre is put to the  
512 middle point of the cell.

513

### 514 **6. Testing the Galperin advection algorithm**

#### 515 **6.1. Standard tests**

516 A set of basic tests and comparison with some classical approaches has been presented by  
517 Galperin (1999) and P08 for the original scheme, along with Bott, Holmgren, and several  
518 other schemes. Their main conclusions were that the scheme is very good for sharp-edge  
519 patterns: in particular, it transports delta functions without any distortions. It had, however,  
520 issues with long slopes, smooth shapes, etc, where the tendency to gradually convert them to a  
521 collection of rectangles was noticeable.

525 Addressing these concerns, tests used during the scheme improvements and implementation  
526 in SILAM included puff-over-background, conical and sin-shaped peaks and dips, etc (some  
527 examples are shown in Figure 2); divergent 1-D high-Courant wind test [in 1-D divergent wind](#)  
528 [field \(Figure 5\)](#), constant-level background field in eight vortices with stagnation points  
529 [\(Figure 6\)](#), and rotation tests for various shapes [\(Figure 7\)](#).

Deleted: Figure 3

Deleted: Figure 4

Deleted: Figure 5

Deleted: -

530 The scheme stays stable at arbitrarily high Courant numbers and handles the [convergence](#) and  
531 divergence of the flows [\(Figure 5\)](#).

Deleted: Figure 3

532 Transport and rotation tests of the improved scheme maintain low distortions of the shapes:  
533 the  $L_2$  norm of the error varies from 0.1% up to 3.8% of the initial-shape norm – for the most  
534 challenging task in [Figure 7](#). The effect of the improvements in comparison with the original  
535 scheme is demonstrated in Figure 2, where the blue contours show the results of the original  
536 scheme. In particular, application of the smoothing Eq. (20) reduced the distortions of  
537 smooth shapes (red curves), largely resolving the concerns of P08: Figure 2b presents the  
538 same test as one of the P08 exercises. However, the smoother also leads to a certain numerical  
539 viscosity of the scheme, so its use in problems requiring non-diffusive schemes (e.g., narrow  
540 plumes from accidental releases) should be avoided.

Deleted: Figure 5

541 The test with eight vortices was difficult for the original scheme [\(Figure 6a\)](#) due to its  
542 insufficient sub-grid resolution but the improvements (15) - [\(16\)](#), section 0, resolved the  
543 problem [\(Figure 6b\)](#). This refinement is instrumental for complex-topography domains.

Deleted: Figure 4

Deleted: (16

Deleted: Figure 4

## 544 **6.2. Global 2-D tests**

545 Performance of Galperin's advection scheme in global spherical domain was assessed with  
546 the collection of demanding tests of (Lauritzen et al. 2012). The cases are designed to evaluate  
547 the accuracy of transport schemes at a wide range of resolutions and Courant numbers. The  
548 tests used a prescribed non-divergent 2D velocity field defined on a sphere and consisting of

558 deformation and rotation, so that the initial concentration pattern is reconstructed at the end of  
559 the test,  $t=T$ , providing the exact solution  $\varphi(t=0) = \varphi(t=T)$ .

560 Four initial concentration distributions were used (Figure 8): “Gaussian hills” with unity  
561 maximum value, “cosine bells” with background of 0.1 and maxima of 1, “slotted cylinders”  
562 – rough pattern with 0.1 background and 1 maximum level, and “correlated cosine bells” –  
563 distribution obtained from “cosine bells” with a function:

564 (27) 
$$\varphi_{ccb} = 0.9 - 0.8\varphi_{cb}^2$$

565 The tests were run with SILAM on a global regular non-rotated lon-lat grid, with  $R=6400$  km  
566 and  $T=12$  h. Spatial resolutions were: 6, 3, 1.5, 0.75, 0.375, and 0.1875 degrees, each run with  
567 mean Courant numbers of  $\sim 5.12$ ,  $\sim 2.56$ ,  $\sim 0.85$  (for  $6^\circ$  grid they correspond to the model time  
568 step of  $T/12=1$ h,  $T/24=30$ min, and  $T/72=5$ min), total 18 runs for each initial pattern.

569 Examples of the most challenging runs with slotted cylinders at  $t=T/2$  and at  $t=T$  are shown in

570 Figure 9 and Figure 10, respectively. The corresponding error fields are collected in Figure 11,

571 as decimal logarithms of the absolute difference between the corresponding field in Figure 10,

572 and the slotted-cylinder initial shape of Figure 8. The main complexity of the test was in

573 reproducing the very tiny sharp-edge structures obtained from the cylinder cut at  $t=T/2$  – and

574 then returning them back by  $t=T$ . The pictures, together with the error field at  $t=T$  (Figure 11)

575 show that already 24 time steps allow the scheme to make the shape recognisable ( $3^\circ$ ,  $C=5.12$

576 pattern), whereas 48 time steps allow for main details to show up. Expectedly, certain

577 deviations at the cylinder edge remain at any resolution – as visible from the error fields.

578 Deviation of the resulting field  $\varphi_r = \varphi(t=T)$  from the initial shape  $\varphi_0 = \varphi(t=0)$ , was

579 considered in three spaces:  $L_2$ ,  $L_\infty$ ,  $L_1$ . The corresponding distance metrics are defined as

580 follows:

Deleted: Figure 6

Deleted: 26

Deleted: Figure 7

Deleted: Figure 8

Deleted: Figure 9

Deleted: Figure 8

Deleted: Figure 6

Deleted: Figure 9

589 (28) 
$$l_2 = \left[ \frac{S[(\varphi_T - \varphi_0)^2]}{S[\varphi_0^2]} \right]^{1/2}, \quad l_\infty = \frac{\max |\varphi_T - \varphi_0|}{\max \varphi_0}, \quad l_1 = \left[ \frac{S[|\varphi_T - \varphi_0|]}{S[|\varphi_0|]} \right]$$

Deleted: 27

590 where  $S[\cdot]$  is an area-weighted sum over latitude and longitude. The values of these three  
 591 metrics for all model runs are presented in [Figure 12](#). The main interest of these curves is that  
 592 they show the rate of the scheme convergence (straight grey lines correspond to the first- and  
 593 second-order convergence rates). Expectedly, the rates depend on the transported shape (the  
 594 smoother the shape the faster convergence) and on the norm used. Thus, the scheme  
 595 converges in  $L_1$  faster than in  $L_2$ , whereas in  $L_\infty$  no convergence in case of sharp edges is an  
 596 expected result. The rate in the  $L_2$  norm is in-between the first- and the second order, whereas  
 597 in  $L_1$  it is close to the latter one.

Deleted: Figure 10

598 Advection should also keep the local ratio of the tracer's concentrations. Such ratio between  
 599 "cosine bells" and "correlated cosine bells" was calculated at  $t=T/2$  and  $t=T$ . Since these  
 600 initial patterns are related by eq. (27), the concentration fields during the tests should maintain  
 601 the same relation. The scatter plots of the concentrations in these two tests give an indication  
 602 on how the ratio is kept. Ideal advection would keep all points on a line given by Eq. (28).  
 603 The results of the tests for  $t=T/2$  are shown in [Figure 13](#), where the results with and without  
 604 the smoother in Eq. (20) are presented. The smoother improves the scheme linearity, i.e. it can  
 605 be recommended to chemical composition computations, which usually also tolerate some  
 606 numerical viscosity.

Deleted: (26

Deleted: (27

Deleted: Figure 11

Deleted: ing

Deleted: (21

### 607 6.3. Global 3-D test with real wind

608 Testing the scheme with real-wind conditions has one major difficulty: there is no accurate  
 609 solution that can be used as a reference. An exception is simulations of constant-mixing-ratio  
 610 3D field, which, once initialised, must stay constant throughout the run. Deviation from this  
 611 constant is then the measure of the model quality. Such test verifies both the scheme and the  
 612 meteo-to-dispersion interface, which has to provide the consistent wind fields.

620 The constant-vmr test was set with winds taken from ERA-Interim archive of ECMWF, for an  
621 arbitrarily selected month of January 1991 ([Figure 15](#)). The model was initialised with vmr =  
622 1 and run with 3° of lon-lat resolution and time step of 30 minutes (max Courant number  
623 exceeding 13 in the stratosphere and reaching up to 2-3 in the troposphere). The model top  
624 was closed at 10Pa, which corresponds to the top level of the ERA-Interim fields. The  
625 procedure described in the section 5.3 was used to diagnose the vertical wind component.  
626 The results of the test are shown in [Figure 15](#), which depicts the model state after 240 hours  
627 of the run, panel a) showing the [boundary-layer](#) vmr, and panel b) presenting it in the  
628 stratosphere. The zonally-averaged vertical cross-section is shown in panel c. Green colours  
629 in the pictures correspond to less than 1% of the instant-field error.

630 An important message is that the limited distortions about 1-2% are visible in a few places but  
631 they are not related to topography, rather being associated with the frontal zones and  
632 cyclones. The comparatively coarse spatial and temporal resolution of the test makes the  
633 associated changes of the wind quite sharp, so that the dimension-split errors start manifesting  
634 themselves. Smoother flows in the stratosphere posed minor challenges for the scheme. [The](#)  
635 [L2-error \(not shown\) is approximately proportional to the model time step.](#)

## 637 7. Discussion

638 The presented SILAM v.5 transport module is based on semi-Lagrangian advection scheme of  
639 M. Galperin with subgrid information available through the positions of centres of masses. It  
640 poses certain challenges in implementation. Firstly, one has to organise the sub-grid  
641 information use and transmission between the advection and other model units. Secondly, the  
642 scheme requires storage of four full fields for each transported species (mass and moments)  
643 and care should be taken to maintain an efficient exchange between the processors and the

Deleted: Figure 12

Deleted: Figure 12

Deleted: near-surface

### Deleted: [Efficiency of Galperin advection scheme](#)

Evaluation of the scheme efficiency is always very difficult as it depends on computer, parallelization, compiler options, etc. Nevertheless, some basic characteristics of the scheme have been deduced from comparison of the simple cases for classical schemes (Galperin 2000). It was shown to be 2.3 - 15 times faster than, e.g., Bott scheme depending on implementation, specific test, etc.

For the L14 tests, the run with 0.75 degree resolution and 120 time steps (took 47 seconds) can be related to performance of HEL and CSLAM schemes, which were tested against the same collection by (Kaas et al. 2013). With all ambiguity of the runtime parameter, it took about 200 seconds for HEL and 300 seconds for CSLAM, i.e. about 4 and 6 times longer than for SILAM. Our tests were run on a simple notebook with dual-core hyperthreaded Intel Core i5-540M CPU and 4G of RAM (Intel Linpack = 18.5 GFlops; memory bandwidth = 7.2 GB/s, according to STREAM <http://www.cs.virginia.edu/stream/benchmark>). We used GNU compiler with -O3 optimization without parallelization, which corresponds to the settings of (Kaas et al. 2013).

In SILAM applications, advection is parallelised using the shared-memory OMP technology, whereas the MPI-based domain split is being developed. The OMP parallelization is readily applicable along each dimension, thus exploiting the dimensional split of the advection scheme. For MPI, care should be taken to allow for a sufficient width of the buffer areas to handle the Courant > 1 cases.

The original scheme was formulated for the bulk mass of all transported tracers, thus performing the advection step for all species at once: the tracer's mass in the slab definition (5) was the sum of masses of all species. This algorithm is faster than the species-wise advection and reduces the number of the moments per dimension down to one regardless the number of tracers. It can also be useful in case of strong chemical binds between the species in coarse-grid and sub-optimal Courant number: as seen from Figure 11, such runs can have noticeable non-linearity between the tracer concentrations. The bulk advection does not have the non-linearity problem but instead loses much of its quality if the species have substantially different lifetimes in the atmosphere, are emitted from substantially different sources or otherwise decorrelated in space.

710 computer memory. Thirdly, possibility to run with high Courant numbers and MPI  
711 parallelization via horizontal domain split can be utilised only if the MPI split allows for  
712 sufficient buffer zones. Finally, the better performance of the advection at Courant number  
713 greater than 1 challenges the implementation of other modules, first of all, chemistry and  
714 emission. Indeed, introduction of emitted mass once per long time step would result in a  
715 broken plume unless the mass is spread downwind over the corresponding distance. Similar  
716 problems show up in chemical transformation calculations. At present, the actual SILAM  
717 applications are performed with Courant close to but mostly smaller than one to avoid such  
718 problems.

Deleted: of the domain

719 The above challenges are mostly technical and their solution allows the scheme to  
720 demonstrate strong performance with low computational costs.

721 In particular, by attributing the release from point source to its actual location one can reduce  
722 the impact of the common problem of Eulerian models: point release is immediately diluted  
723 over the model grid cell. This substantially improves the transport though does not solve the  
724 problem completely: (i) the chemical module still receives the diluted plume concentration,  
725 (ii) the slab size in case of the source near the centre of the grid cell will still be as large as the  
726 grid cell itself. A more accurate solution would be the plume-in-grid or similar approaches,  
727 which is being built in SILAM. Another example of the sub-grid information usage is  
728 utilisation of full meteorological vertical resolution to calculate effective values of meteo  
729 variables for thick dispersion layers (Sofiev 2002).

730 The model can operate at any Courant number (Figure 5). Its time step is limited not by grid  
731 cell size but by a spatial scale of the wind-shear field, i.e. has to satisfy much less restrictive  
732 Lipschitz criterion, which relates spatial and temporal truncation errors (Pudykiewicz et al.  
733 1985). It follows from the advection step (6) and the reprojection step (8), which do not

Deleted: Figure 3

Deleted: (6

737 restrict new positions of the slabs: they can find themselves anywhere in the grid or outside it  
738 after the time step is made.

739 SILAM heavily relies on such features of Galperin's scheme as mass conservation and  
740 accountability: the scheme provides complete mass budget including transport across the  
741 domain boundaries. In particular, nesting of the calculations is straightforward and does not  
742 need the relaxation buffer at the edges of the inner domain: the inflow through the boundaries  
743 is described by the same slabs as the main advection. The scheme is also shape-preserving –  
744 in the sense this term is used by L14, – i.e. it does not result in unphysical solutions, such as  
745 negative mixing ratio. Some distortions are still possible (Figure 2), which can be reduced by  
746 the smoother described in section 4.4, eq. ( 20).

### 747 **7.1. Standard advection tests**

748 Evaluating the Galperin's scheme with the simple tests (Figure 2 - [Figure 7](#)), one can point  
749 out the known issues of the classical schemes resolved in Galperin's approach: high-order  
750 algorithms suffer from numerical diffusion, oscillations at sharp gradients (require special  
751 efforts for limiting their amplitude), high computational costs and stringent limits to Courant  
752 number. None of these affect the Galperin scheme.

753 The main issue noticed during the implementation of the original scheme was the  
754 unrealistically high concentrations near the wind stagnation points. Thus, the concentration  
755 pattern at the test [Figure 6a](#) resembles the situation of divergent wind field. However, it is not  
756 the case: the 2D wind pattern is strictly solenoidal. The actual reason is insufficient resolution  
757 of the advection grid: one centre of mass point is not enough if spatial scale of the wind  
758 variation is comparable with the grid cell size. Tracking the edges of the slab rather than its  
759 centre resolves the problem ([Figure 6b](#)).

Deleted: Figure 5

Deleted: Figure 4

Deleted: Figure 4

763 The other challenging tasks for Galperin’s algorithm were those with smooth background and  
764 soft gradients, a frequent issue for semi-Lagrangian schemes, which is easily handled by more  
765 diffusive approaches. This feature was visible in the P08 tests where the scheme noticeably  
766 distorts the Gaussian and conical plumes. For the puff-over-background pattern, the scheme  
767 makes a single low-mass dip in the vicinity of the puff, which receives this mass (Figure 2).  
768 From formal point of view, the scheme does not conserve the higher moments inside the grid  
769 cell, which becomes a problem when the pattern changes at a spatial scale shorter than the  
770 grid cell size. The smoothing step (20) may be advised despite it has no rigorous ground and,  
771 as in L14 evaluation of other schemes, may damage some formal quality scores (adding this  
772 step introduces numerical viscosity - Figure 2).

## 7.2. *Global 2D and real-wind advection tests*

773 The application of the scheme to highly challenging tests of (Lauritzen et al. 2012) allowed its  
774 evaluation in a global 2-D case and comparison with the state-of-the-art schemes evaluated by  
775 L14 and (Kaas et al. 2013).

776 Performing these tests with different spatial and temporal resolutions, as well as Courant  
777 numbers, suggested that the scheme has an “optimal” Courant number for each spatial  
778 resolution where the error metrics reach their minimum, so that the increase of temporal  
779 resolution where the error metrics reach their minimum, so that the increase of temporal  
780 resolution is not beneficial. Indeed, in [Figure 12](#), the low-Courant runs are by no means the  
781 most accurate. This is not surprising: for an ideal scheme, increasing the grid resolution and  
782 reducing the time step should both lead to gradual convergence of the algorithm, i.e. the error  
783 metrics should reduce. For real schemes, higher temporal resolution competes with  
784 accumulation of the scheme errors with increasing number of steps. Convergence in L14 tests  
785 was still solid for all fixed-Courant-number series ([Figure 12](#)) but excessive temporal  
786 resolution (specific for each particular grid cell size) was penalised by higher errors.

787 Similarly, the most-accurate representation of the correlated patterns is obtained from the runs

Deleted: Figure 10

Deleted: Figure 10

790 with the intermediate Courant numbers (Figure 13). This seems to be a common feature: the  
791 same behaviour was noticed by L14 for several schemes.

Deleted: Figure 11

792 High optimal Courant numbers, however, should be taken with care. For L14, the smooth  
793 wind fields reduced the dimension-split error and made the long time steps particularly  
794 beneficial.

Deleted:

795 It is also seen (Figure 11) that the best performance, in case of near-optimal Courant, is  
796 demonstrated by the high-spatial-resolution simulations, which have reproduced both the  
797 sharp edges of the slotted cylinders, the flat background and the cylinder's top planes.

Deleted: Figure 9

798 The scheme demonstrated convergence rate higher than one for all metrics and all tests with  
799 smooth initial patterns. Even for the most-stringent test with the slotted cylinders, the scheme  
800 showed the first-order convergence rate in the  $L_1$  norm (Figure 12).

Deleted: i

Deleted: s

Deleted: Figure 10

801 Among the other features of the solution, one can notice a certain inhomogeneity of the  
802 background field away from the transported bodies. The error is very small ( $< 10^{-4}$ ) for high-  
803 resolution cases (Figure 11) and  $< 0.1\%$  for inexpensive setups, such as  $\Delta\lambda=0.75$ ,  $C=2.56$ . For  
804 coarser resolutions, it grows. The inhomogeneity also grows with Courant number, which is  
805 opposite to decreasing error of representation of the shapes themselves. The issue originates  
806 from the dimension-split error in polar areas, where the spatial scale of wind change becomes  
807 comparable with the distance passed by the slabs within one time step.

808 Similar non-monotonicity of background is visible for some schemes tested by L14.

809 Unfortunately, no error fields are given there but Figs. 7-10 there are comparable with our  
810 Figure 9 (results without smoother). With few exceptions (schemes TTS-I and LPM, notations  
811 of L14), all algorithms manifested such patterns unless filters are applied. For some schemes  
812 (SFF-CSLAM3, SFF-CSLAM4, UCISOM-CS, CLAW, and CAM), these inhomogeneities  
813 are visible also for the tests with shape-preserving filters. One should note however that the

820 0.1 level, which distinguishes between the two violet colours in Figure 9 and Fig. 7-10 of L14,  
821 corresponds to the background level in slotted-cylinder test. As a result, even a very small  
822 deviation leads to appearance of such shapes in the plots (note stripes in background of Figure  
823 8).

824 Comparing the so-called “minimal resolution” threshold for  $L_2$  norm of cosine bells to reach  
825 0.033 (Figure 3 of L14) for SILAM was about  $0.75^\circ$ , which puts it in the middle of that multi-  
826 model chart (specific place depends on whether the shape preservation is considered or not).

827 Another criterion can be the optimal convergence of  $L_2$  and  $L_\infty$  norms for Gaussian hills:

828 about 1.7-1.8 for SILAM – is again in the middle of the L14 histograms, in the second half if  
829 the unlimited schemes (without shape-preservation filters) are considered and in the first half  
830 if the unphysical negative concentrations are suppressed (since the Galperin advection is  
831 strictly positively defined, no extra efforts needed to satisfy this requirement).

832 Interestingly, the L14 tests were limited with  $3^\circ$  as the coarsest resolution, and it was pointed  
833 out that the schemes start converging only when a certain limit, specific for each scheme, is  
834 reached. The SILAM results show similar behaviour only for the lowest Courant number (red  
835 lines in Figure 12), which indeed required appropriate resolution to start working. Higher-  
836 Courant setups were much less restrictive (the errors decrease with growing resolution also  
837 for coarse-grids) and, as already pointed out, often worked better than the low-Courant runs  
838 (similar to many L14 schemes).

839 The scheme demonstrated limited distortion of pre-existing functional dependence – see the  
840 cosine bells and correlated cosine bells tests, Eq ( 27) (Figure 13). Formal scores suggested by  
841 (Lauritzen et al. 2012a) calculated for the Galperin scheme are shown in Figure 14. Notations  
842 are:  $l_o$ , “overshooting”, describes the values that fell outside the rectangular [0.1:1] (Figure  
843 13),  $l_u$ , “shape-preserving unmix”, describes the values inside that rectangular but outside the

Deleted: it with other schemes tested by L14 can be made along several lines. For instance,

Deleted: around centre

Deleted: addressed

Deleted: e

Deleted: do not

Deleted: such

Deleted: : the errors decrease with growing resolution started from the coarsest grids – except

Deleted: Figure 10

Deleted: also

Deleted: non-linearity

858 “lens” formed by its diagonal  $(0.1, 1) - (1, 0.1)$  and the curve, and  $l_r$ , “real mixing”, describes  
859 the values inside the “lens”. Comparison with L14 (Fig. 15, middle panel) shows that the  
860 Galperin scheme outperforms CLAW, SLFV-ML, SLFV-SL, and all setups of ICON  
861 schemes, being close to CAM-SE, MIPAS, and HOMME, and trailing behind the runs with  
862 CSLAM, HEL, SFF, and UCISCOM schemes.

863 A peculiarity of the mixing diagnostic scores is that they are significantly affected by the  
864 background areas far from the advected bells, which occupy only a small fraction of the  
865 domain (Figure 8). As a result, small background fluctuations discussed above in application  
866 to slotted cylinders (see error field in Figure 11) contribute significantly to the mixing  
867 diagnostic scores too. In particular, the high-Courant simulations, which accurately reproduce  
868 the bells themselves (the dots are close to the curve in the scatter-plots Figure 13), still show  
869 poor formal scores due to non-zero width of the cloud near the location  $(0.1, 1)$ , where all  
870 background dots should arrive. This issue contributes most-significantly into “overshooting”  
871 part of the error, but also to other two components.

872 Expectedly, the smoother improves the mixing diagnostic scores, mainly affecting the  
873 representation of the bells themselves (Figure 13). This is in contrast with the schemes tested  
874 in L14, where the shape-preservation filters mostly removed the penalty for overshooting the  
875 background but rarely improved the other two components, sometimes worsening them.

876 Following the conclusions of the section 4.4 and 1D tests, we used the smoothing factor of  
877 0.08, which is a compromise between the scheme diffusivity and distortion reduction. As a  
878 result, some non-linearity exists also in the smoothed solution. The test showed that simple  
879 increase of temporal resolution leads to increase of the number of steps and related  
880 reprojections, which then worsen the representation of the bells – but improved the  
881 background field by reducing the dimension-split errors. A synchronous rise of the resolution

**Deleted:** Its best setups are favourably comparable with majority of the schemes tested in L14, especially if the versions with the shape-preservation filters are considered (and chemical transformation modules are usually sensitive to negative masses). Interestingly

**Deleted:** ing step (20)

**Deleted:** scheme linearity

**Deleted:** Figure 11

**Deleted:** –

**Deleted:** to the

**Deleted:** damaged the linearity

895 in time and space with the same Courant number (columns in Figure 13) showed better results  
896 for higher-resolving setups.

897 Further investigating the flat-field behaviour in complex wind pattern, the simulations with  
898 the constant-vmr initial conditions (Figure 15) were performed, showing that the model has  
899 no major problem in keeping the homogeneous distribution: deviations do not exceed few %  
900 with no relation to topography. The existing ups and downs of the vmr are related to cyclones  
901 and atmospheric fronts, which challenge the dimension-splitting algorithm rather than the  
902 core 1D advection (it transports the homogeneous field perfectly – no distortion was found  
903 after  $10^5$  steps regardless the Courant number). Increasing the resolution leads to lower  
904 “unmix” of the pattern (not shown). This experiment refines the “optimal-Courant”  
905 recommendation of the L14 test, which had smoother wind fields and, consequently, higher  
906 optimal Courant number. For real-life applications, especially with coarse grid, it may be  
907 necessary to choose time step short enough to ensure comparable levels of time- and space-  
908 wise truncation errors (Pudykiewicz et al. 1985). This case also argues for developing the 2D  
909 implementation of Galperin scheme, which would eliminate the horizontal dimension split.

### 7.3. Where to use the smoother

911 When deciding of whether to apply the smoother Eq ( 20), one has to keep in mind that  
912 Galperin scheme is always positively defined and does not need a shape-preserving filter to  
913 provide a “physically meaningful” solution, i.e. without negative values. It is free from this  
914 caveat. The purpose of the smoother is only to reduce the non-linear distortions of fields.  
915 The smoother has both positive and negative impact on the scheme performance. Among the  
916 positive ones are: (i) it damps the distortions of smooth shapes and gradients (section 4.4), (ii)  
917 it reduces the amplification factor precluding it from exceeding one even for few time steps  
918 (section 4.5), (iii) it reduces the unmixing problem (Figure 14). Its negative features are: (i)  
919 the obtained solution is diffusive (section 4.4), (ii) moderate and high frequencies in the

Deleted: T

Deleted: Figure 12

Deleted: ed

Deleted: already with Courant number just above one, owing to the coarse spatial resolution

Deleted: s

Deleted: keep it less than one

928 solution spectrum are damped (section 4.5), (iii) formal scores and convergence rates are  
929 lower in some tests (sections 6.2 and 7.2). The smoother has little impact on background  
930 inhomogeneity.  
931 Most of positive and negative features coincide with impact of shape-preserving filters (e.g.,  
932 L14), despite the different idea and formulations.  
933 Since the smoother computational cost is negligible, one can decide whether to apply it  
934 depending only on the problem at hands. Strict interconnections between the species, smooth  
935 patterns and tolerance to diffusion form a case for the smoother. Conversely, sharp plumes  
936 over zero background (e.g., accidental release case) argue against it.  
937 The smoother impact grows monotonically with its parameter  $\epsilon$ . Numerous tests showed that  
938 the distortions and above-one amplification factor essentially disappear at  $\epsilon \sim 0.08$ , where the  
939 diffusivity also becomes significant. This value appeared stable with regard to Courant  
940 number and setup of the tests.

#### 941 **7.4. Efficiency of Galperin advection scheme**

942 Evaluation of the scheme efficiency is always very difficult as it strongly depends on the  
943 algorithm implementation, but also on computer, parallelization, compiler options, etc.  
944 Nevertheless, basic characteristics of the scheme can be deduced from comparison of its  
945 original version with several classical schemes made by Galperin (2000). It included, in  
946 particular, EM72 and Bott, which appeared  $>5$  and  $>3$  times slower, respectively. Comparison  
947 with another implementation of Bott routine by (Petrova et al. 2008) showed 7-15 times  
948 difference depending on tests. The updated scheme version, however, is bound to be heavier.  
949 It is also worth putting it in line with modern approaches.  
950 In this section, the efficiency of the updated Galperin scheme is evaluated from several points  
951 of view: (i) the scalability with regard to the number of transported species, spatial and

952 temporal resolution, specifics of the problem at hands, (ii) comparison with “standard  
953 implementation” of the Bott algorithm and semi-Lagrangian scheme, (iii) comparison of the  
954 runtime in the L14 tests with HEL and CSLAM schemes.

#### 955 **7.4.1.SILAM run time vs number of species, temporal and** 956 **spatial resolution**

957 The scalability of the scheme and the whole SILAM model was tested in real-wind global  
958 simulations for arbitrarily taken three days (15-17.5.2012). The reference run was set with  
959 0.5° resolution, 6 vertical layers, time step of 30 minutes, and one aerosol species. Two types  
960 of emission were considered: an artificial one-hour-long source filling-up the whole 3D  
961 domain, and the SILAM-own wind-blown dust emission model, which created dust plumes  
962 from sandy areas of Sahara. Vertical diffusion, which is coupled with vertical 1D advection,  
963 was turned off for artificial source test but turned on for dust source in order to allow the  
964 model to quickly populate the upper layers of the domain. Then, the number of aerosol  
965 species, spatial and temporal resolutions were repeatedly doubled (one change at a time).  
966 The model was run in a single-processor mode but compiled with O3 optimization and OMP  
967 code pre-processing. Runs were made in a notebook with Intel Core i7 processor and repeated  
968 in a workstation with Intel Xeon E5. The scaling differed by 10-20%, which was considered  
969 to be negligible.

970 The results (Figure 16) highlight the scalability of the scheme and its implementation in  
971 SILAM. The species-unrelated time of horizontal 2D advection (Figure 16a, offset in  
972 regression line) is ~30% of a single-species computation time (represented via slope). This  
973 “overhead” is, in fact, the transport-step integrals Eq. ( 17) - ( 19), which are computed only  
974 once and used for all species. Higher overhead of the vertical advection is due to necessity to  
975 handle the uneven vertical layers, which makes it scaling just 20% better than 2D horizontal  
976 one. It also has larger species-independent overhead.

977 With chemical module turned off, advection constitutes ~85% of the total model run time.  
978 Since the scheme operates with the source grid cells, it can check that  $M_i^n > 0$  before going  
979 into computations, which gives a very substantial speed-up in case of limited-volume plumes  
980 (Figure 16b). In Saharan dust run, the horizontal advection time is about-twice lower, whereas  
981 the vertical advection, even together with diffusion, becomes all but negligible, owing to  
982 efficient filtering of zero-columns in comparison with lon- or lat- stripes.  
983 A faster-than-proportional growth of the horizontal advection time with increasing resolution  
984 (Figure 16c, normalised run time) is a result of growing Courant number: for 4-times smaller  
985 grid cell (0.25° lon-lat resolution) the time step of 30 minutes means  $C \gg 1$  over large part of  
986 the domain. As a result, transport integrals Eq. ( 17) - ( 19) have to be analysed over longer  
987 paths. Still, the growth is much smaller than the cost of 4-fold reduction of time step, which  
988 makes the high-C computations attractive. Vertical advection is not affected and its time is  
989 proportional to the number of columns to analyse.  
990 Time spent by advection is practically proportional to the temporal resolution (Figure 16c),  
991 i.e. it follows the number of times the advection is computed in the run.

#### **7.4.2. Comparison with efficiency of other schemes**

992 Comparison with other schemes is arguably the most-uncertain part of the exercise: the  
993 scheme efficiency is strongly dependent on the quality of the implementation (note the  
994 different results for Bott scheme obtained by Galperin, (2000) and (Petrova et al. 2008)). To  
995 obtain reproducible results, we made this comparison against the “standard implementation”  
996 of the Bott code available from internet ([http://www2.meteo.uni-](http://www2.meteo.uni-bonn.de/forschung/gruppen/tgwww/people/abott/fortran/fortran_english.html)  
997 bonn.de/forschung/gruppen/tgwww/people/abott/fortran/fortran\_english.html, visited  
998 28.09.2015). Since our code is also available (see section 8), this comparison is reproducible.

1000 The test with  $10^4$  time steps, 2000 gridpoints in 1D periodic grid, Courant number = 0.1, and  
1001 one species took: 0.92 sec for Galperin scheme (~0.3 sec for cell border advection, ~0.6 sec  
1002 for slab reprojection) and 0.85 sec for Bott scheme. This confirms the expectation that the  
1003 updates of the Galperin scheme from its initial version about-tripled its run time, which is  
1004 now similar to that of the Bott scheme. However, the Galperin scheme still scales better with  
1005 the number of species: as shown in previous section, only reprojection is multiplied with the  
1006 number of species, whereas Bott scheme does not have such saving possibility.

1007 The above numbers should be considered as indicative only since the environment for the  
1008 tests was completely artificial: the schemes were used as a stand-alone code applied in 1D  
1009 space. Galperin scheme needed only one moment instead of three, which would be the case of  
1010 3D advection. Despite very limited extra computations, this would still raise the memory  
1011 exchange. The Bott scheme was taken without shape-preservation filter, which would be  
1012 needed for any real-life applications.

1013 The tests were also made for our own implementation of the semi-Lagrangian scheme (took  
1014 ~50% longer than the above timing) but its efficiency was not carefully verified.

1015 The L14 tests allowed rough benchmarking of the SILAM implementation of the scheme in  
1016 2D tasks. In particular, the run with  $0.75^\circ$  resolution and 120 time steps can be related to  
1017 performance of HEL and CSLAM schemes, which were tested against the same test collection  
1018 by (Kaas et al. 2013). Extrapolating the charts of Fig. 13 of (Kaas et al. 2013) to one species  
1019 (the range given there is 2-20 species), the test takes about 190 seconds for HEL and 300  
1020 seconds for CSLAM but only 47 seconds for SILAM, i.e. the difference was about 4 and 6  
1021 times, respectively.

1022 Formal benchmarks of the computers, the main uncertainty in this comparison, are essentially  
1023 the same: Kaas et al used Intel Core2 Duo E6550 processor (Intel Linpack 20 GFlops,

1024 <http://www.techpowerup.com>, visited 8.10.2015). Our tests were run on a simple notebook  
1025 [with mobile Intel Core i5-540M Duo \(Intel Linpack 18.5 GFlops\)](#). These CPUs were also  
1026 [compared in http://www.cpubenchmark.net](http://www.cpubenchmark.net) (visited 8.10.2015), which also put them within  
1027 [20% from each other](#), albeit i5-540M was put forward. Memory bandwidth of our notebook,  
1028 [as always for compact computers](#), was modest: 7.2 GB/s (STREAM test,  
1029 <http://www.cs.virginia.edu/stream/ref.html> accessed 5.10.2015). We used GNU compiler with  
1030 [-O3 optimization without parallelization](#), similar to [Kaas et al. \(2013\)](#).

Deleted: (

### **7.4.3. Further boosting the scheme efficiency: parallelization**

1031 [In SILAM applications, advection is parallelised using the shared-memory OMP technology,](#)  
1032 [whereas the MPI-based domain split is being developed.](#) The OMP parallelization is readily  
1033 [applicable along each dimension, thus exploiting the dimensional split of the advection](#)  
1034 [scheme.](#) For MPI, care should be taken to allow for a sufficient width of the buffer areas to  
1035 [handle the Courant > 1 cases.](#)

1037 [The original scheme was formulated for the bulk mass of all transported tracers, thus](#)  
1038 [performing the advection step for all species at once: the tracer's mass in the slab definition \(](#)  
1039 [5\) was the sum of masses of all species. This is much faster than the species-wise advection](#)  
1040 [and reduces the number of the moments per dimension down to one regardless the number of](#)  
1041 [tracers. It is also useful in case of strong chemical binds between the species because the bulk](#)  
1042 [advection keeps all pre-existing relations between the species. However, transport accuracy](#)  
1043 [diminishes if the species have substantially different life times in the atmosphere, are emitted](#)  
1044 [from substantially different sources or otherwise decorrelated in space.](#)

1045

1047 **8. Code availability**

1048 SILAM is a publicly available model. Our experience shows however that its successful  
1049 application critically depends on the user's modelling skills and understanding of the model  
1050 concepts. Therefore, SILAM is available on-request basis from the authors of this paper, who  
1051 also provide support in the initial model installation and setup. The model description,  
1052 operational and research products, as well as reference documentation, are presented at

1053 <http://silam.fmi.fi> (accessed 5.10.2015). The model user's guide is available at

1054 [http://silam.fmi.fi/doc/SILAM\\_v5\\_userGuide\\_general.pdf](http://silam.fmi.fi/doc/SILAM_v5_userGuide_general.pdf) (accessed 5.10.2015). Potential

1055 model users and also encouraged to refer to the SILAM Winter School material at

1056 [http://silam.fmi.fi/open\\_source/SILAM\\_school/index.htm](http://silam.fmi.fi/open_source/SILAM_school/index.htm) (accessed 5.10.2015).

1057 The stand-alone code of Galperin advection scheme used in above 1D tests, is available at

1058 [http://silam.fmi.fi/open\\_source/public/advection\\_Galperin\\_stand\\_alone.zip](http://silam.fmi.fi/open_source/public/advection_Galperin_stand_alone.zip).

1059

1060 **9. Summary**

1061 Current paper presents the transport module of System for Integrated modeLling of

1062 Atmospheric coMposition SILAM v.5, which is based on the improved advection routine of

1063 Michael Galperin combined with separate developments for vertical diffusion and dry

1064 deposition.

1065 The corner stone of the advection scheme is the subgrid information on distribution of masses

1066 inside the grid cells, which is generated at the emission calculation stage and maintained in a

1067 consistent way throughout the whole model, including chemical transformation, deposition,

1068 and transport itself. This information, albeit requiring substantial storage for handling, allows

1069 for accurate representation of transport.

Deleted: 2

Deleted: 6

Deleted: 2

Deleted: 6

Deleted: 2

Deleted: 6

Deleted: s

Deleted: are

1078 The scheme is shown to be particularly efficient for point sources and sharp gradients of the  
1079 concentration fields, still showing solid performance for smooth patterns. The most  
1080 challenging task was found to be the puff-over-plain test, where the scheme showed  
1081 noticeable distortions of the concentration pattern. Application of a simple smoother  
1082 efficiently reduces the problem at a cost of non-zero viscosity of the resulting scheme.

1083 Advanced tests and comparison with state-of-art algorithms confirmed the compromise  
1084 between the efficiency and accuracy. SILAM performance was fully comparable with the  
1085 other algorithms, outperforming some of them.

1086 Among the future developments, implementation of the scheme in 2D space and replacement  
1087 of the smoother with extensions of the core advection algorithm, are probably the most-  
1088 pressing ones.

**Deleted:** introduction of physically grounded horizontal diffusion procedure

1089

## 1090 **10. Acknowledgments**

1091 The development of the SILAM model was supported by ASTREX project of Academy of  
1092 Finland, as well as by ESA-ATILA and FP7-MACC projects. The authors thank late Dr.Sci.  
1093 M.Galperin for the original version of the scheme, Dr. A.Bott for the publicly available  
1094 version of his scheme, and Dr.Kaas and an anonymous reviewer for detailed comments of the  
1095 manuscript.

1096

## 1097 **11. References**

1098 Bott, A., 1989. A positive definite advection scheme obtained by nonlinear renormalization of  
1099 the advective fluxes. *Monthly Weather Review*, 117(5), pp.1006–1016. Available at:  
1100 [http://siba.unipv.it/fisica/articoli/M/Monthly Weather Rev\\_vol.117\\_1989\\_pp.1006-](http://siba.unipv.it/fisica/articoli/M/Monthly Weather Rev_vol.117_1989_pp.1006-1015.pdf)  
1101 [1015.pdf](http://siba.unipv.it/fisica/articoli/M/Monthly Weather Rev_vol.117_1989_pp.1006-1015.pdf) [Accessed September 8, 2011].

- 1104 Bott, A., 1992. Monotone flux limitation in the area - preserving flux form advection  
1105 algorithm. *Monthly Weather Review*, 120, pp.2592–2602.
- 1106 Bott, A., 1993. The monotone area - preserving flux - form advection algorithm: reducing the  
1107 time - splitting error in two - dimensional flow fields. *Monthly Weather Review*, 121,  
1108 pp.2637–2641.
- 1109 Charney, J.G., FJortoft, R. & Neumann, J. Von, 1950. Numerical Integration of the  
1110 Barotropic Vorticity Equation. *Tellus A*, 2(4), pp.238–254.
- 1111 Crowley, W.P., 1968. Numerical advection experiments. *Monthly Weather Review*, 96(1),  
1112 pp.1–11.
- 1113 Crowley, W.P., 1967. Second order numerical advection. *Journal of Computational Physics*,  
1114 1(4), pp.474–474.
- 1115 Egan, B.A. & Mahoney, J.R., 1972. Numerical Modeling of Advection and Diffusion of  
1116 Urban Area Source Pollutants. *Journal of Applied Meteorology*, 11, pp.312–322.  
1117 Available at: <http://adsabs.harvard.edu/abs/1972JApMe..11..312E> [Accessed September  
1118 8, 2011].
- 1119 Galperin, M. et al., 1994. *Model evaluation of airborne Trace Metal transport and deposition.*  
1120 *Short model description and preliminary results.*, Moscow.
- 1121 Galperin, M. V, 1999. Approaches for improving the numerical solution of the advection  
1122 equation. In Z. Zlatev, ed. *Large-Scale Computations in Air Pollution Modelling, Proc.*  
1123 *NATO Advanced Research Workshop on Large Scale Computations in Air Pollution*  
1124 *Modelling, Sofia, Bistrizta.* Sofia: Kluwer Academic Publishers, Dordrecht, The  
1125 Netherlands., pp. 161–172.
- 1126 Galperin, M. V, 2000. The Approaches to Correct Computation of Airborne Pollution  
1127 Advection. In *Problems of Ecological Monitoring and Ecosystem Modelling. XVII (in*  
1128 *Russian).* St.Petersburg: Gidrometeoizdat, pp. 54–68.
- 1129 Galperin, M. V & Sofiev, M., 1995. Evaluation of airborne heavy-metal pollution from  
1130 European sources. *INTERNATIONAL JOURNAL OF ENVIRONMENT AND*  
1131 *POLLUTION*, 5(4-6), pp.679–690.
- 1132 Galperin, M. V & Sofiev, M., 1998. The long-range transport of ammonia and ammonium in  
1133 the Northern Hemisphere. *ATMOSPHERIC ENVIRONMENT*, 32(3), pp.373–380.
- 1134 Galperin, M. V, Sofiev, M. & Afinogenova, O., 1995. Long-term modelling of airborne  
1135 pollution within the Northern Hemisphere. *WATER AIR AND SOIL POLLUTION*, 85(4),  
1136 pp.2051–2056.
- 1137 Galperin, M. V, Sofiev, M. & Cheshukina, T. V, 1997. An approach to zoom modelling of  
1138 acid deposition on the basis of sulfur compound evaluation for the St. Petersburg region.  
1139 *INTERNATIONAL JOURNAL OF ENVIRONMENT AND POLLUTION*, 8(3-6), pp.420–  
1140 426.

- 1141 Ghods, A., Sobouti, F. & Arkani-Hamed, J., 2000. An improved second moment method for  
1142 solution of pure advection problems. *International Journal for Numerical Methods in*  
1143 *Fluids*, 32(8), pp.959–977. Available at: [http://doi.wiley.com/10.1002/\(SICI\)1097-](http://doi.wiley.com/10.1002/(SICI)1097-0363(20000430)32:8<959::AID-FLD995>3.0.CO;2-7)  
1144 [0363\(20000430\)32:8<959::AID-FLD995>3.0.CO;2-7](http://doi.wiley.com/10.1002/(SICI)1097-0363(20000430)32:8<959::AID-FLD995>3.0.CO;2-7).
- 1145 Heimann, M. & Keeling, C., 1989. A three-dimensional model of atmospheric CO<sub>2</sub> transport  
1146 based on observed winds: 2. Model description and simulated tracer experiments.  
1147 *Geophysical Monograph*, 55, pp.237–275.
- 1148 Kaas, E. et al., 2013. A hybrid Eulerian–Lagrangian numerical scheme for solving prognostic  
1149 equations in fluid dynamics. *Geoscientific Model Development*, 6(6), pp.2023–2047.  
1150 Available at: <http://www.geosci-model-dev.net/6/2023/2013/> [Accessed April 4, 2014].
- 1151 Kaas, E. & Nielsen, J.R., 2010. A Mass-Conserving Quasi-Monotonic Filter for Use in Semi-  
1152 Lagrangian Models. *Monthly Weather Review*, 138(5), pp.1858–1876. Available at:  
1153 <http://journals.ametsoc.org/doi/abs/10.1175/2009MWR3173.1>.
- 1154 Kokkola, H. et al., 2008. SALSA – a Sectional Aerosol module for Large Scale Applications.  
1155 *Atmospheric Chemistry and Physics*, 8(9), pp.2469–2483. Available at:  
1156 <http://www.atmos-chem-phys.net/8/2469/2008/>.
- 1157 Kouznetsov, R. & Sofiev, M., 2012. A methodology for evaluation of vertical dispersion and  
1158 dry deposition of atmospheric aerosols. *Journal of Geophysical Research*, 117(D01202).
- 1159 Kreiss, H.O. & Olinger, J., 1972. Comparison of accurate methods for integration of hyperbolic  
1160 equation. *Tellus A*, XXIV(2), pp.199–215.
- 1161 Kukkonen, J. et al., 2012. A review of operational, regional-scale, chemical weather  
1162 forecasting models in Europe. *Atmospheric Chemistry and Physics*, 12(1), pp.1–87.  
1163 Available at: <http://www.atmos-chem-phys.net/12/1/2012/> [Accessed January 3, 2012].
- 1164 Lauritzen, P., Ullrich, P. & Nair, R., 2011. Atmospheric Transport Schemes: Desirable  
1165 Properties and a Semi-Lagrangian View on Finite-Volume Discretizations. In P.  
1166 Lauritzen et al., eds. *Numerical Techniques for Global Atmospheric Models SE - 8*.  
1167 Lecture Notes in Computational Science and Engineering. Springer Berlin Heidelberg,  
1168 pp. 185–250. Available at: [http://dx.doi.org/10.1007/978-3-642-11640-7\\_8](http://dx.doi.org/10.1007/978-3-642-11640-7_8).
- 1169 Lauritzen, P.H. et al., 2012. A standard test case suite for two-dimensional linear transport on  
1170 the sphere. *Geoscientific Model Development*, 5(3), pp.887–901. Available at:  
1171 <http://www.geosci-model-dev.net/5/887/2012/> [Accessed April 2, 2014].
- 1172 Lauritzen, P.H. et al., 2014. A standard test case suite for two-dimensional linear transport on  
1173 the sphere: results from a collection of state-of-the-art schemes. *Geoscientific Model*  
1174 *Development*, 7(1), pp.105–145. Available at: [http://www.geosci-model-](http://www.geosci-model-dev.net/7/105/2014/)  
1175 [dev.net/7/105/2014/](http://www.geosci-model-dev.net/7/105/2014/) [Accessed April 2, 2014].
- 1176 Van Leer, B., 1974. Towards the Ultimate Conservative Difference Scheme. II. Monotonicity  
1177 and Conservation Combined in a Second-Order Scheme. *Journal of Computational*  
1178 *Physics*, 14, pp.361–370.

- 1179 Van Leer, B., 1977. Towards the Ultimate Conservative Difference Scheme. IV. A New  
1180 Approach to Numerical Convection. *Journal of Computational Physics*, 23, pp.276–299.
- 1181 Van Leer, B., 1979. Towards the ultimate conservative difference scheme. V. A second-order  
1182 sequel to Godunov's method. *Journal of Computational Physics*, 32(1), pp.101–136.  
1183 Available at: <http://www.sciencedirect.com/science/article/pii/0021999179901451>  
1184 [Accessed November 1, 2011].
- 1185 Leith, C.E., 1965. Numerical Simulation of the Earth's Atmosphere. In *Methods in*  
1186 *Computational Physics*, vol. 4. NY: Academic Press, pp. 1–28.
- 1187 Leonard, B.P., 2002. Stability of explicit advection schemes. The balance point location rule.  
1188 *International Journal for Numerical Methods in Fluids*, 38(5), pp.471–514. Available at:  
1189 <http://dx.doi.org/10.1002/flid.189>.
- 1190 Lin, S.J. & Rood, R.B., 1996. Multidimensional flux-form semi-Lagrangian transport  
1191 schemes. *Monthly Weather Review*, 124(9), pp.2046–2070. Available at:  
1192 <http://cat.inist.fr/?aModele=afficheN&cpsidt=3197665> [Accessed September 8,  
1193 2011].
- 1194 Lin, S.-J. & Rood, R.B., 1997. An explicit flux-form semi-Lagrangian shallow-water model  
1195 of the sphere. *Quarterly Journal of Royal Meteorological Society*, 123, pp.2477–2498.
- 1196 Lowe, D. et al., 2003. A condensed-mass advection based model for the simulation of liquid  
1197 polar stratospheric clouds. *Atmospheric Chemistry and Physics*, pp.29–38. Available at:  
1198 [www.atmos-chem-phys.net/3/29/2003/](http://www.atmos-chem-phys.net/3/29/2003/).
- 1199 Marchuk, G., 1995. *Adjoint equations and analysis of complex systems*, Kluwer Academic  
1200 Publishers, Dordrecht, The Netherlands.
- 1201 Pedersen, L.B. & Prahm, L.P., 1974. A method for numerical solution of the advection  
1202 equation. *Tellus B*, XXVI(5), pp.594–602.
- 1203 Pepper, D.W. & Long, P.E., 1978. A comparison of results using second-order moments with  
1204 and without width correction to solve the advection equation. *Journal of Applied*  
1205 *Meteorology*, 17, pp.228–233.
- 1206 Petroff, a. & Zhang, L., 2010. Development and validation of a size-resolved particle dry  
1207 deposition scheme for application in aerosol transport models. *Geoscientific Model*  
1208 *Development*, 3(2), pp.753–769. Available at: [http://www.geosci-model-](http://www.geosci-model-dev.net/3/753/2010/)  
1209 [dev.net/3/753/2010/](http://www.geosci-model-dev.net/3/753/2010/) [Accessed November 14, 2013].
- 1210 Petrova, S. et al., 2008. Some fast variants of TRAP scheme for solving advection equation —  
1211 comparison with other schemes. *Computers & Mathematics with Applications*, 55(10),  
1212 pp.2363–2380. Available at:  
1213 <http://linkinghub.elsevier.com/retrieve/pii/S0898122107007304> [Accessed September 8,  
1214 2011].

- 1215 Prahm, L.P. & Christensen, O., 1977. Long range transmission of pollutants simulated by a  
1216 two-dimensional pseudospectral dispersion model. *Journal of Applied Meteorology*, 16,  
1217 pp.896–910.
- 1218 Prather, M. et al., 1987. Chemistry of the global troposphere - Fluorocarbons as tracers of air  
1219 motion. *Journal of geophysical research*, 92, pp.6579–6613.
- 1220 Prather, M.J., 1986. Numerical Advection by Conservation of Second-Order Moments. *J.*  
1221 *Geophys. Res.* 91(D6), pp.6671–6681. Available at:  
1222 [http://www.ess.uci.edu/~prather/publications/1986JGR\\_Prather-SOM.pdf](http://www.ess.uci.edu/~prather/publications/1986JGR_Prather-SOM.pdf) [Accessed  
1223 October 29, 2011].
- 1224 Pudykiewicz, J., Benoit, R. & Staniforth, a., 1985. Preliminary results From a partial LRTAP  
1225 model based on an existing meteorological forecast model. *Atmosphere-Ocean*, 23(3),  
1226 pp.267–303. Available at:  
1227 <http://www.tandfonline.com/doi/abs/10.1080/07055900.1985.9649229> [Accessed April  
1228 6, 2014].
- 1229 Richtmyer, R.D., 1962. *A survey of difference methods for non-steady fluid dynamics*,  
1230 Boulder, CO.
- 1231 Ritchie, H., 1988. Application of the semi-Lagrangian method to a spectral model of the  
1232 shallow water equations. *Monthly Weather Review*, 116(8), pp.1587–1598. Available at:  
1233 [http://www.csa.com/partners/viewrecord.php?requester=gs&collection=ENV&  
1234 recid=8903483](http://www.csa.com/partners/viewrecord.php?requester=gs&collection=ENV&recid=8903483) [Accessed September 8, 2011].
- 1235 Roach, P., 1980. *Computational hydrodynamics*,
- 1236 Robertson, L. & Langner, J., 1999. An Eulerian Limited-Area Atmospheric Transport Model.  
1237 *Journal of Applied Meteorology*, 38(section 3), pp.190–210.
- 1238 Rood, R.B., 1987. Numerical advection algorithms and their role in atmospheric transport and  
1239 chemistry models. *Reviews of geophysics*, 25(1), pp.71–100. Available at:  
1240 [http://www.coaps.fsu.edu/pub/eric/OCP5930/Papers/Rood\\_Numerical\\_Advection.pdf](http://www.coaps.fsu.edu/pub/eric/OCP5930/Papers/Rood_Numerical_Advection.pdf)  
1241 [Accessed September 8, 2011].
- 1242 Rotman, D.A. et al., 2004. IMPACT, the LLNL 3-D global atmospheric chemical transport  
1243 model for the combined troposphere and stratosphere: Model description and analysis of  
1244 ozone and other trace gases. *Journal of Geophysical Research*, 109(D4).
- 1245 Russell, G.L. & Lerner, J.A., 1981. A new finite-differencing scheme for the tracer transport  
1246 equation. *Journal of Applied Meteorology*, 20, pp.1483–1498. Available at:  
1247 <http://adsabs.harvard.edu/abs/1981JApMe..20.1483R> [Accessed November 1, 2011].
- 1248 Seinfeld, J.H. & Pandis, S.N., 2006. *Atmospheric chemistry and physics. From air pollution*  
1249 *to climate change* 2nd ed., John Wiley & sons, Inc, Hoboken, New Jersey.
- 1250 Slinn, W.G.N., 1982. Predictions for particle deposition to vegetative canopies.  
1251 *ATMOSPHERIC ENVIRONMENT*, 16(7), pp.1785–1794.

- 1252 Smagorinsky, J., 1963. General circulation experiments with the primitive equations. I. The  
1253 basic experiment. *Monthly Weather Review*, 91(3), pp.99–164.
- 1254 Smolarkiewicz, P.K., 1982. The multi-dimensional Crowley advection scheme. *Monthly*  
1255 *Weather Review*, 110, pp.1968–1983.
- 1256 Sofiev, M., 2000. A model for the evaluation of long-term airborne pollution transport at  
1257 regional and continental scales. *ATMOSPHERIC ENVIRONMENT*, 34(15), pp.2481–  
1258 2493.
- 1259 Sofiev, M., 2002. Extended resistance analogy for construction of the vertical diffusion  
1260 scheme for dispersion models. *JOURNAL OF GEOPHYSICAL RESEARCH-*  
1261 *ATMOSPHERES*, 107(D12), pp.ACH 10–1–ACH 10–8.
- 1262 Sofiev, M., Galperin, M. V & Genikhovich, E., 2008. Construction and evaluation of Eulerian  
1263 dynamic core for the air quality and emergency modeling system SILAM. In C. Borrego  
1264 & A. I. Miranda, eds. *NATO Science for piece and security Serties C: Environmental*  
1265 *Security. Air pollution modelling and its application, XIX*. SPRINGER-VERLAG  
1266 BERLIN, pp. 699–701.
- 1267 Staniforth, A. & Cote, J., 1991. Semi-Lagrangian Integration Schemes for Atmospheric  
1268 Models – A Review. *Monthly Weather Review*, 119, pp.2206–2223.
- 1269 Syrakov, D., 1996. On the TRAP advection scheme — Description, tests and applications. In  
1270 G. Geernaert, A. Walloe-Hansen, & Z. Zlatev, eds. *Regional Modelling of Air Pollution*  
1271 *in Europe*. Roskilde: National Environmental Research Institute, pp. 141–152.
- 1272 Syrakov, D. & Galperin, M., 1997. On a new BOTT-type advection scheme and its further  
1273 improvement. In H. Hass & I. J. Ackermann, eds. *Proceedings of the first GLOREAM*  
1274 *Workshop*. Aachen, Germany: Ford Forschungszentrum Aachen, pp. 103–109.
- 1275 Syrakov, D. & Galperin, M., 2000. On some explicit advection schemes for dispersion  
1276 modelling applications. *INTERNATIONAL JOURNAL OF ENVIRONMENT AND*  
1277 *POLLUTION*, 14, pp.267–277.
- 1278 Venkatram, A. & Pleim, J., 1999. The electrical analogy does not apply to modeling dry  
1279 deposition of particles. *Atmospheric Environment*, 33(18), pp.3075–3076. Available at:  
1280 <http://linkinghub.elsevier.com/retrieve/pii/S1352231099000941>.
- 1281 Walcek, C.J., 2000. Minor flux adjustment near mixing ratio extremes for simplified yet  
1282 highly accurate monotonic calculation of tracer advection. *Journal of Geophysical*  
1283 *Research*, 105(D7), p.9335. Available at: <http://doi.wiley.com/10.1029/1999JD901142>.
- 1284 Walcek, C.J. & Aleksic, N.M., 1998. A simple but accurate mass conservative, peak-  
1285 preserving, mixing ratio bounded advection algorithm with FORTRAN code.  
1286 *Atmospheric Environment*, 32(22), pp.3863–3880. Available at:  
1287 <http://linkinghub.elsevier.com/retrieve/pii/S1352231098000995>.
- 1288 Wesely, M., 1989. Parameterization of surface resistances to gaseous dry deposition in  
1289 regional-scale numerical models. *Atmospheric Environment*, 23(6), pp.1293–1304.

- 1290 Available at: <http://www.sciencedirect.com/science/article/pii/0004698189901534>  
1291 [Accessed November 1, 2011].
- 1292 Yabe, T. et al., 2001. An Exactly Conservative Semi-Lagrangian Scheme (CIP–CSL) in One  
1293 Dimension. *Monthly Weather Review*, 129(1992), pp. 332–344.
- 1294 Yabe, T. & Aoki, T., 1991. A Universal Solver for Hyperbolic Equations by Cubic-  
1295 Polynomial Interpolation. I. One-dimensional solver. *Computer physics communications*,  
1296 66(2-3), pp.219–232.
- 1297 Yamartino, R.J., 1993. Nonnegative, conserved scalar transport using grid-cell-centered,  
1298 spectrally constrained blackman cubics for applications on a variable-thickness mesh.  
1299 *Monthly Weather Review*, 121, pp.753–763.
- 1300 Yanenko, N.N., 1971. *The method of fractional steps: solution of problems of mathematical*  
1301 *physics in several variables (translated from Russian)*, Berlin: Springer-Verlag Berlin,  
1302 Heidelberg.
- 1303 Zhang, L. et al., 2001. A size-segregated particle dry deposition scheme for an atmospheric  
1304 aerosol module. *ATMOSPHERIC ENVIRONMENT*, 35, pp.549–560.
- 1305 Zlatev, Z. & Berkowicz, R., 1988. Numerical treatment of large - scale air pollution model.  
1306 *Journal of Computational and Applied Mathematics*, 16, pp.93–109.
- 1307
- 1308

1309 **Figure captions**

1310 **Figure 1.** Advection step of the scheme of M.Galperin

1311 **Figure 2.** Shape preservation tests: a) step, b) triangle peak, c) sin-shaped dip, d) sin-shaped peak . Sequential  
1312 positions are shown, 'r' denotes the scheme without smoother, 'r\_diff' – with it. **The legend includes the number**  
1313 **of times steps made. Wind is from left to right, Courant = 0.4.**

Deleted: L

1315 **Figure 3.** Spectral analysis for 1D. Panels a,d) Amplification Factor (AF) and RMSE, respectively for the  
1316 Galperin scheme without smoother; b),e) AF and RMS for Galperin scheme with large background; c), f) AF and  
1317 RMSE for Galperin scheme with smoother  $\epsilon=0.08$ .

1319 **Figure 4.** Example of input and output spectra for broadband input to the advection schemes with zero and  
1320 nonzero background level. Left panels: exact and numerical solutions. Right panels: power spectrum densities  
1321 initially and after one revolution. Top:  $B=0$ , bottom:  $B=1.0$ .

1323 **Figure 5.** Linear-motion tests with a constant-release point source at  $X_0$  and varying wind speed along  $x$ -axis.  
1324 Upper panel: Courant number, lower panel: concentration [arbitrary unit]. Wind blows from left to right.  
1325 Without smoother.

Deleted: 3

Deleted: n [arbitrary unit]. Wind blows from left to right.

1328 **Figure 6.** Test with eight non-divergent 2-D vortices. Left panel: test of the original scheme (5) - (7), time step  
1329 8; right panel: improved scheme (15) - (16), time step 50. Both tasks were initialised with constant value 0.4,  
1330 also used as boundary conditions. Without smoother.

Deleted: 4

Deleted: (5)

Deleted: (16)

Deleted: Both tasks were initialised with constant value 0.4, also used as boundary conditions.

Deleted: 5

1332 **Figure 7.** Double-vortex rotation tests for: a rectangular split between the vortices (upper panels); three single-  
1333 cell peaks and two connected rectangles (middle panels); sin- and cone- shaped surfaces (lower panels). A series  
1334 of time steps shown in the left panels, except for the low panel (shown  $t=361$ ). Right panels: error field after 1  
1335 full revolution (obs 10-fold more sensitive scale and relative L2 norm given above each plot). Max Courant  $\sim$   
1336 1.5. Grid dimensions =  $400 \times 200$ . Without smoother.

1338 **Figure 8.** Initial shapes of the puffs for the 2-D global test on the sphere.

Deleted: 6

1340 **Figure 9.** Half-period ( $t=T/2$ ) shapes for the 2D global test with slotted cylinders for different spatial and  
1341 temporal resolutions. Without smoother.

Deleted: 7

1343 **Figure 10.** Final shapes ( $t=T$ ) for the 2-D global tests with slotted cylinders for different spatial and temporal  
1344 resolutions. Without smoother.

Deleted: 8

Deleted: s

1346 **Figure 11.** The error fields for the final shapes of Figure 10 as compared with slotted cylinder initial shape in  
1347 Figure 8. Without smoother.

Deleted: 9

Deleted: Figure 8

Deleted: Figure 6

1349 **Figure 12.** Dependence of the performance metrics  $l_1$ ,  $l_2$ , and  $l_\infty$  for the spherical 2D tests with initial shapes of  
1350 Figure 8. Dashed straight lines mark the slope for the first and second order of convergence. Without smoother.

Deleted: 10

Formatted: Font: Not Bold

1352 **Figure 13.** Mixing preservation test for cosine bells and correlated cosine bells (27) at  $t=T/2$ . Each two lines  
1353 show the tests without (upper line) and with (lower line) smoother (20).

Deleted: Figure 6

Deleted: 11

Deleted: Linearity

Deleted: (26)

1379 **Figure 14.** A histogram of mixing diagnostic (stacked) for the same resolutions, Courant number and smoother  
1380 factor as in Figure 13. Metrics are (see text and (Lauritzen et al. 2012) for more details):  $L_r$  is “real mixing”,  $L_p$  is  
1381 “range-preserving unmixing”,  $L_o$  is “overshooting”. Values are relative to the reference CSLAM performance in  
1382 L14 tests. Picture is comparable with panel b) of Fig. 15 in L14.

Formatted: Font: Not Bold

1383 **Figure 15.** Constant-vmr test with real-wind conditions after 122 hrs. a) vmr within boundary layer, b) vmr  
1384 above the tropopause, c) zone-average vertical cross-section of vmr. Without smoother.

Deleted: 12

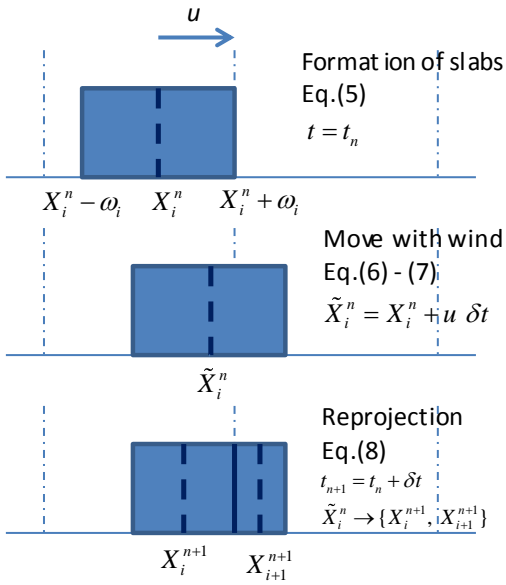
Deleted: near the surface

1386 **Figure 16.** Scalability of Galperin advection scheme and SILAM model. Panel a) Full-grid runtime for different  
1387 number of species, b) sparse-plume run time for different number of species, c) full-grid run time for varying  
1388 horizontal grid resolution, d) full-grid run time for varying time step.

1390

1391

1394



1395

1396

1397

1398

1399

1400

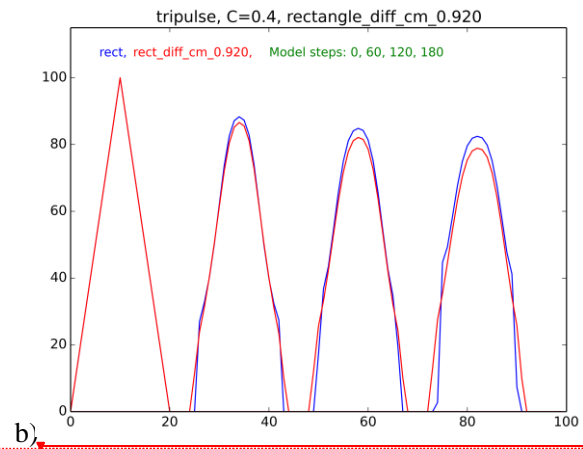
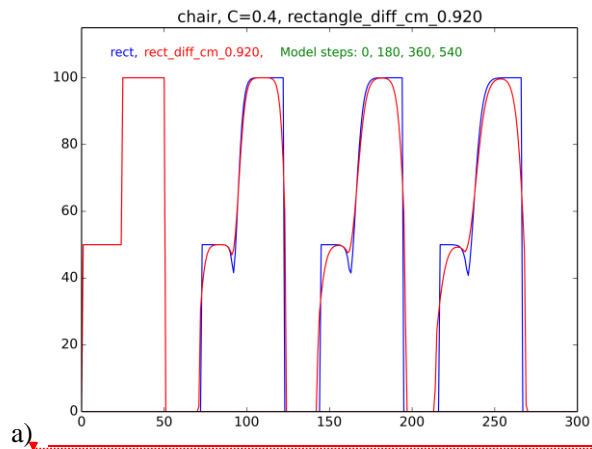
Figure 1. Advection step of the scheme of M. Galperin

1401

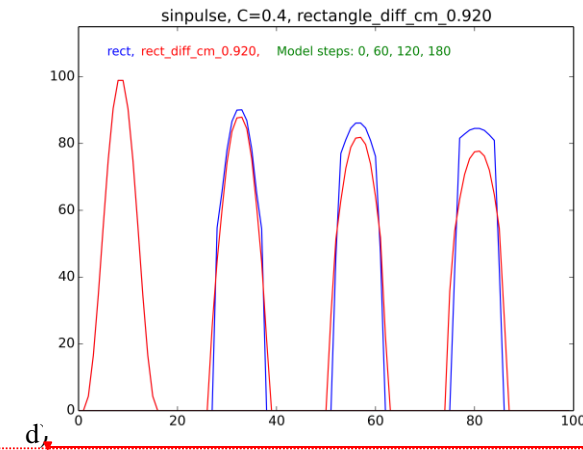
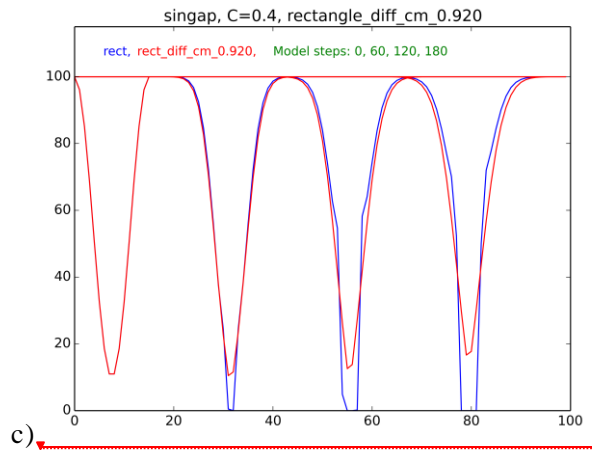
Formatted: Font: Not Bold

Deleted: Figure 1. Advection step of the scheme of M. Galperin

1404



1405



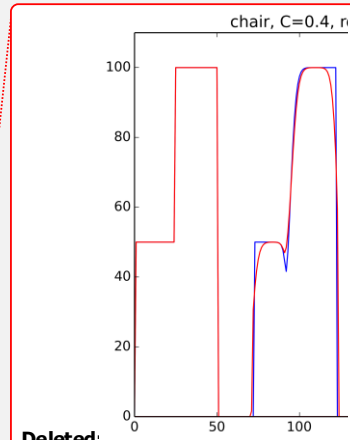
1406

Figure 2. Shape preservation tests: a) step, b) triangle peak, c) sin-shaped dip, d) sin-shaped peak. Sequential positions are shown, 'r' denotes

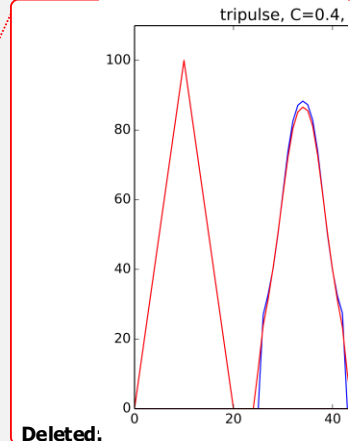
1407

the scheme without smoother, 'r diff' – with it. The legend includes the number of times steps made. Wind is from left to right, Courant = 0.4.

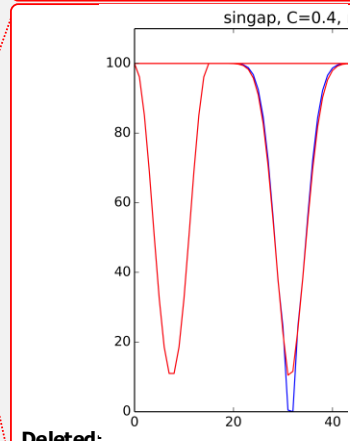
50



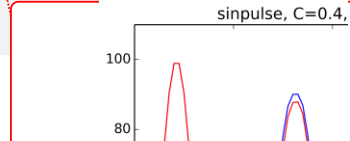
Deleted:



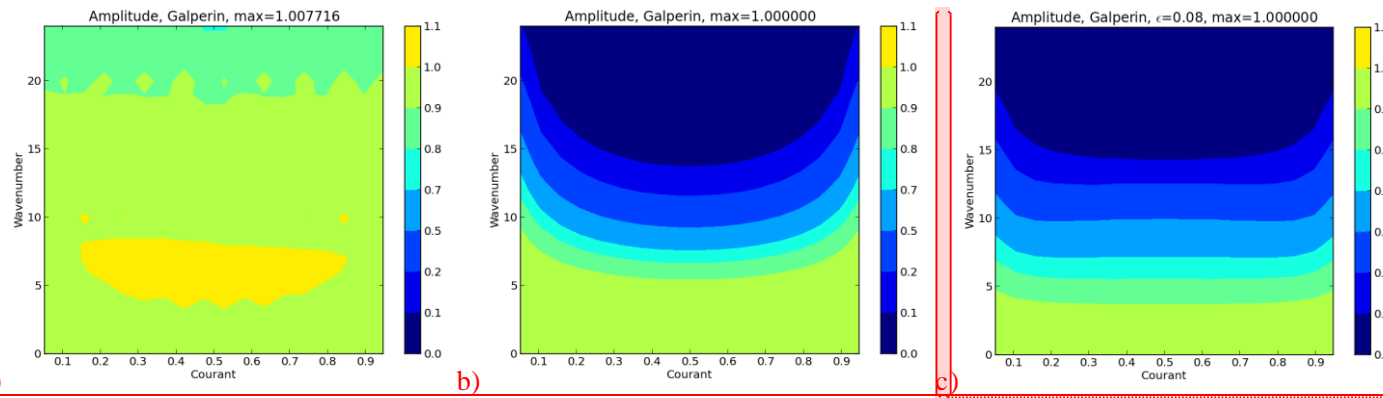
Deleted:



Deleted:

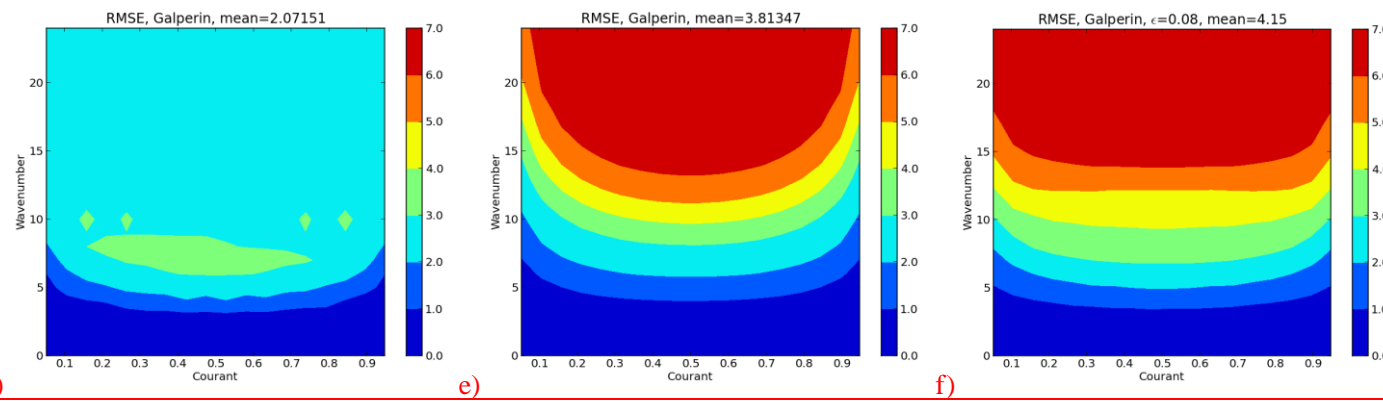


1430



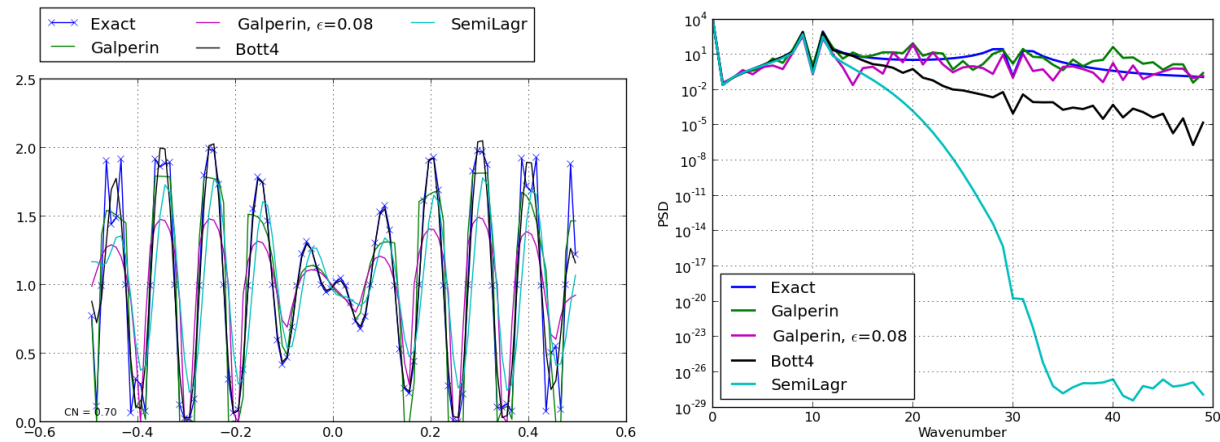
**Comment [MS1]:** May be, scale for the application factor should contain 1 as a edge.

1431

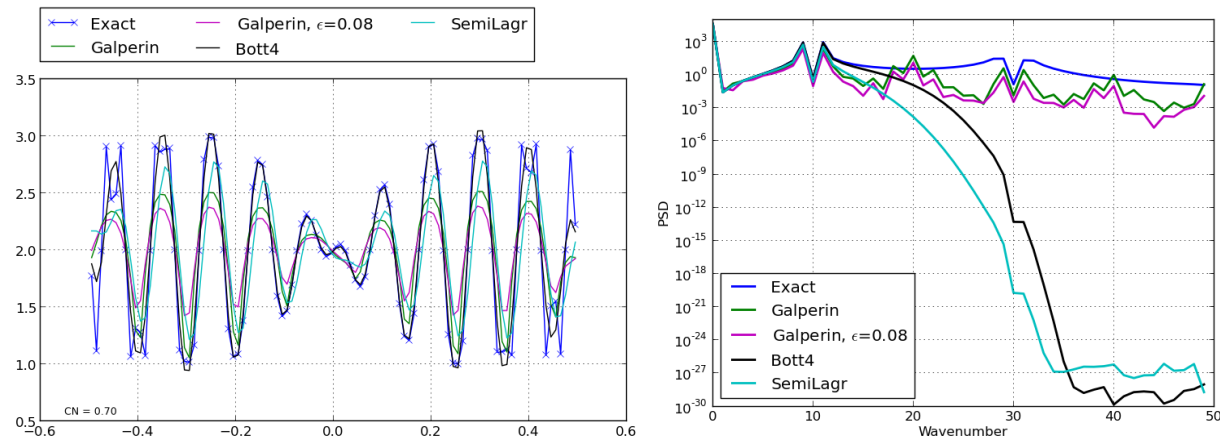


1432

1433 **Figure 3. Spectral analysis for 1D. Panels a),d) Amplification Factor (AF) and RMSE, respectively for the Galperin scheme without**  
1434 **smoother; b),e) AF and RMS for Galperin scheme with large background; c), f) AF and RMSE for Galperin scheme with smoother**  
1435  **$\epsilon=0.08$ .**



1436



1437

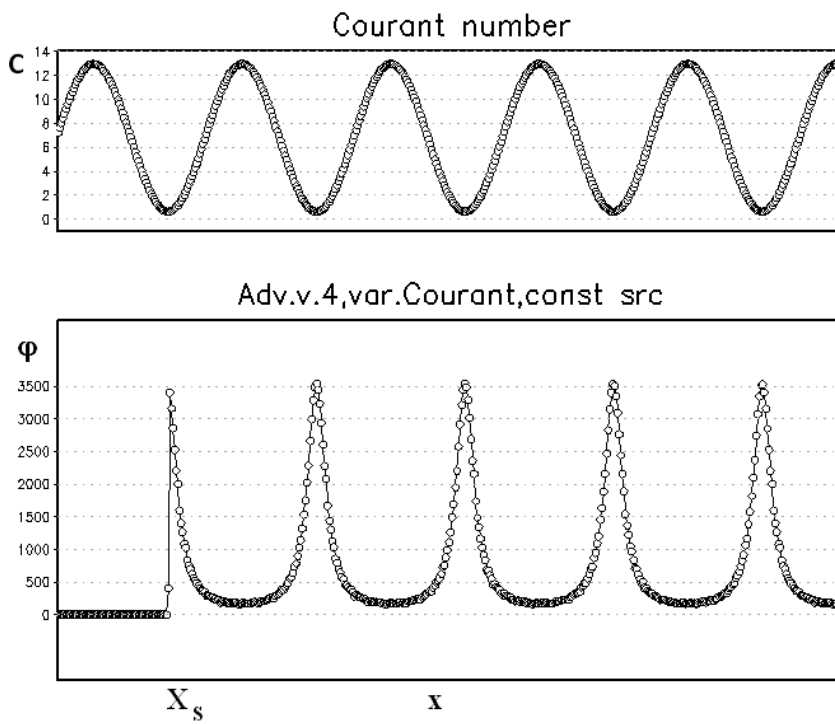
1438 **Figure 4. Example of input and output spectra for broadband input to the advection schemes with zero and nonzero background level.**

1439 **Left panels: exact and numerical solutions. Right panels: power spectrum densities initially and after one revolution. Top:  $B=0$ ,**

1440 **bottom:  $B=1.0$ .**

1441

1442



1443

1444

1445 **Figure 5. Linear-motion tests with a constant-release point source at  $X_s$  and varying wind**

1446 **speed along  $x$ -axis. Upper panel: Courant number, lower panel: concentration**

1447 **[arbitrary unit]. Wind blows from left to right. Without smoother,**

1448

1449

**Deleted:** Figure 3. Linear-motion tests with a constant-release point source at  $X_s$  and varying wind speed along  $x$ -axis. Upper panel: Courant number, lower panel: concentration

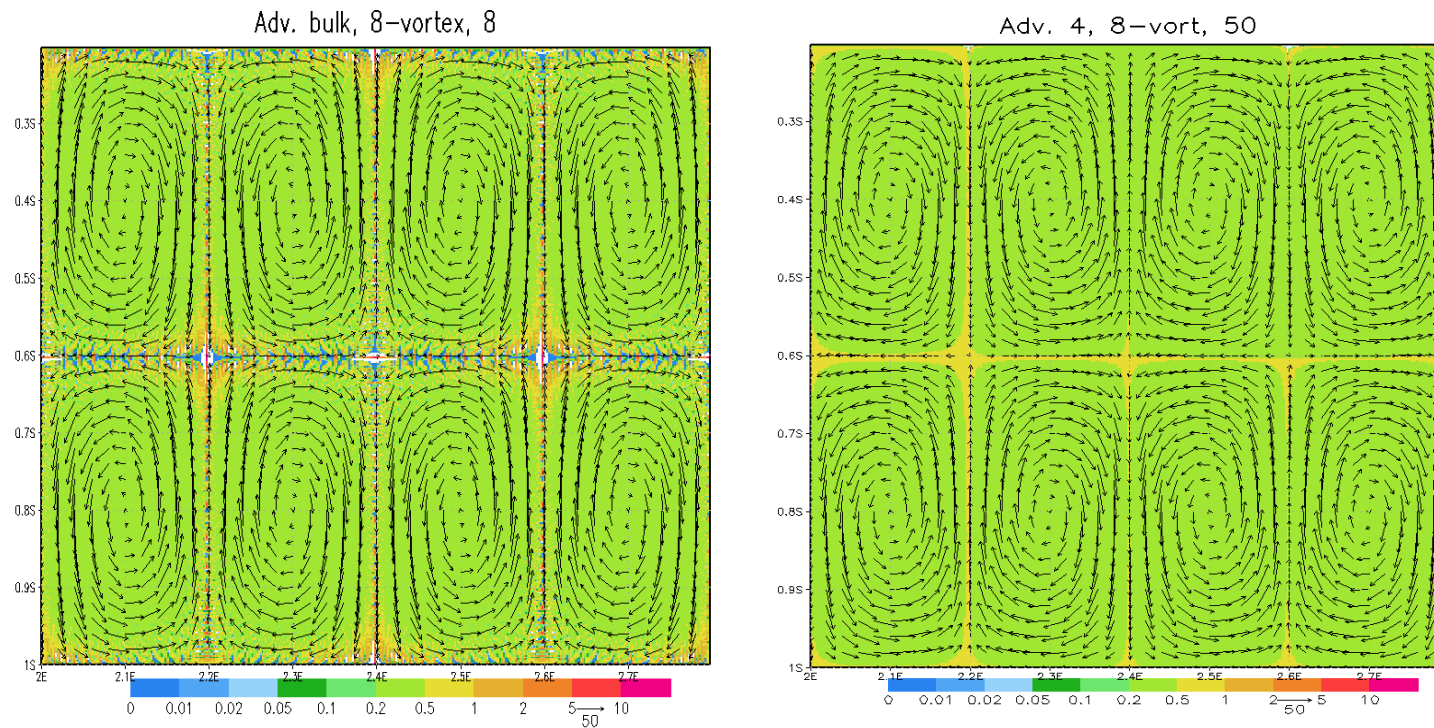


**Figure 6. Test with eight non-divergent 2-D vortices. Left panel: test of the original scheme (5) - (7), time step 8; right panel: improved scheme (15) - (16), time step 50. Both tasks were initialised with constant value 0.4, also used as boundary conditions. Without smoother,**

**Deleted:** Figure 4. Test with eight non-divergent 2-D vortices. Left panel: test of the original scheme (5) - (7), time step 8; right panel: improved scheme (15) - (16), time step 50.

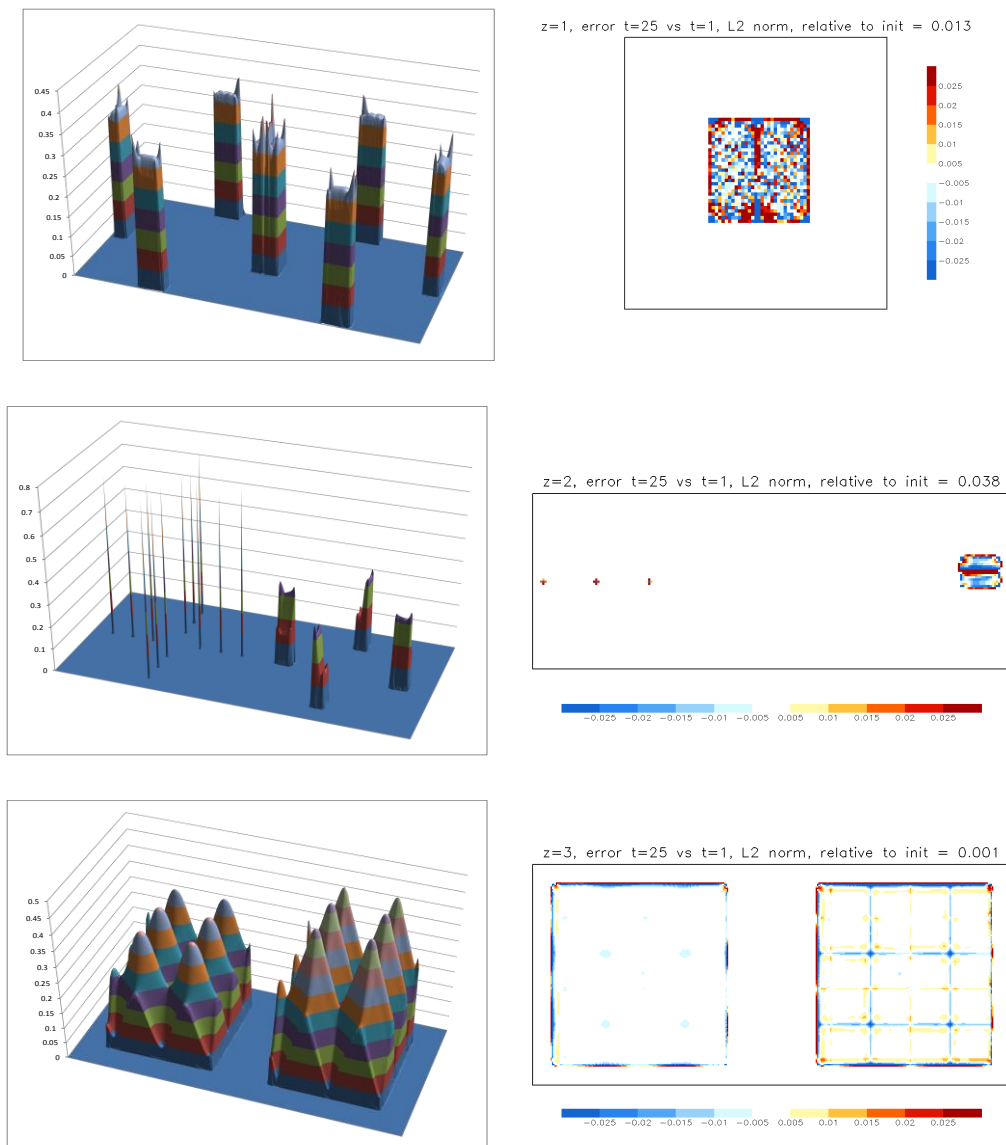


Figure 7. Double-vortex rotation tests for: a rectangular split between the vortices (upper panels); three single-cell peaks and two connected rectangles (middle panels); sin- and cone-shaped surfaces (lower panels). A series of time steps shown in the left panels, except for the low panel (shown  $t=361$ ). Right panels: error field after 1 full revolution (obs 10-fold more sensitive scale and relative L2 norm given above each plot). Max Courant  $\sim 1.5$ . Grid dimensions =  $400 \times 200$ . Without smoother.

Formatted: Font: Not Bold

Formatted: Font: Not Bold

~~Deleted:~~ Figure 5. Double-vortex rotation tests for: a rectangular split between the vortices (upper panels); three single-cell peaks and two connected rectangles (middle panels); sin- and cone-shaped surfaces (lower panels). A series of time steps shown in the left panels, except for the low panel (shown  $t=361$ ). Right panels: error field after 1 full revolution (obs 10-fold more sensitive scale and relative L2 norm given above each plot). Max Courant  $\sim 1.5$ . Grid dimensions =  $400 \times 200$ .

Formatted: Font: Not Bold

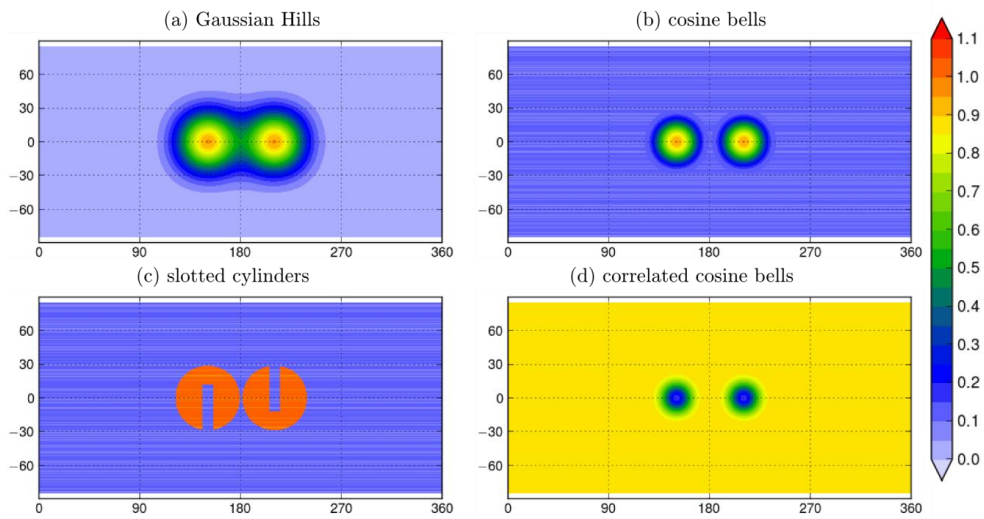


**Figure 8. Initial shapes of the puffs for the 2-D global test on the sphere.**

**Deleted:** Figure 6. Initial shapes of the puffs for the 2-D global test on the sphere.

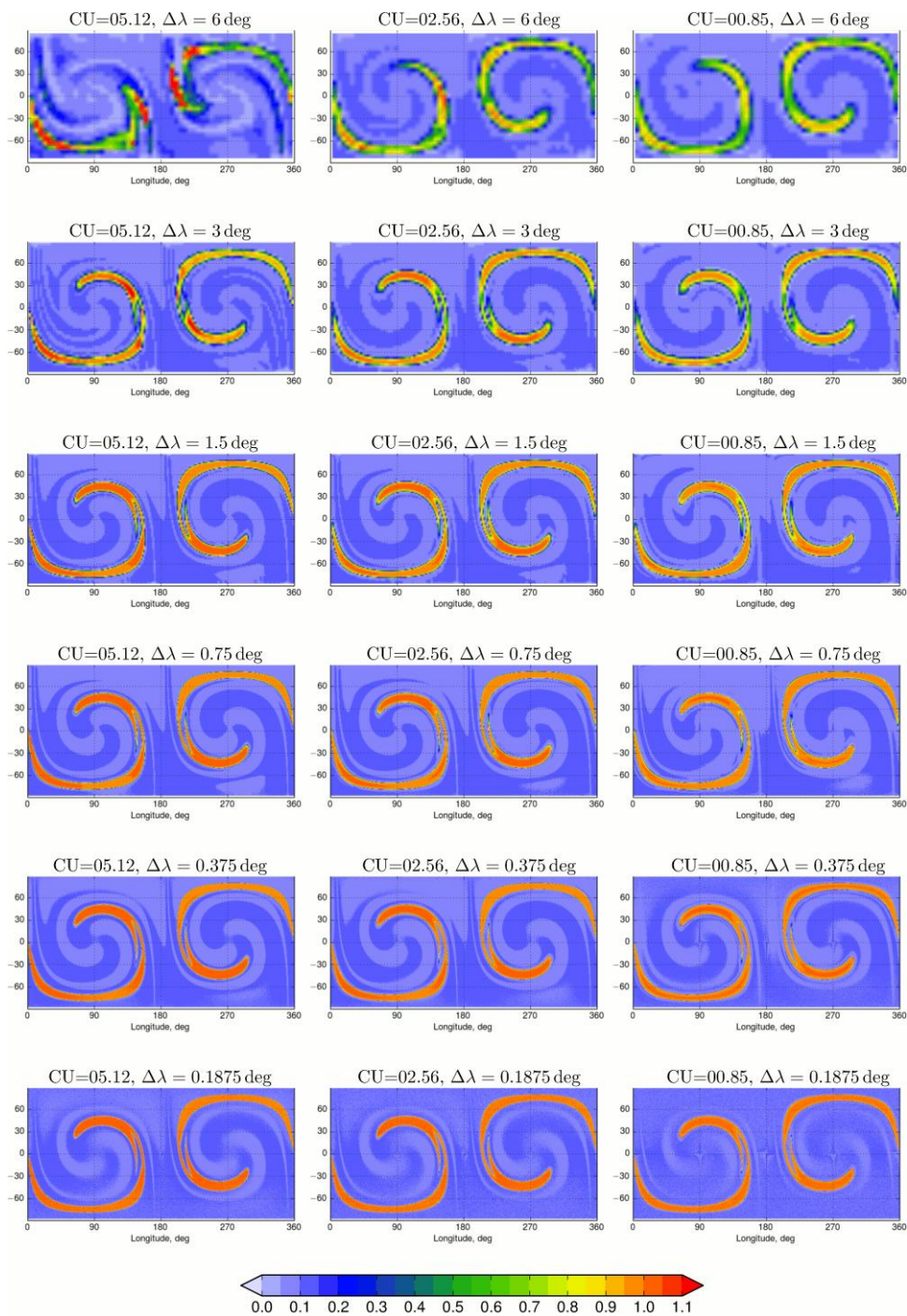


**Figure 9. Half-period ( $t=T/2$ ) shapes for the 2D global test with slotted cylinders for different spatial and temporal resolutions. Without smoother.**

**Deleted:** Figure 7. Half-period ( $t=T/2$ ) shapes for the 2D global test with slotted cylinders for different spatial and temporal resolutions.

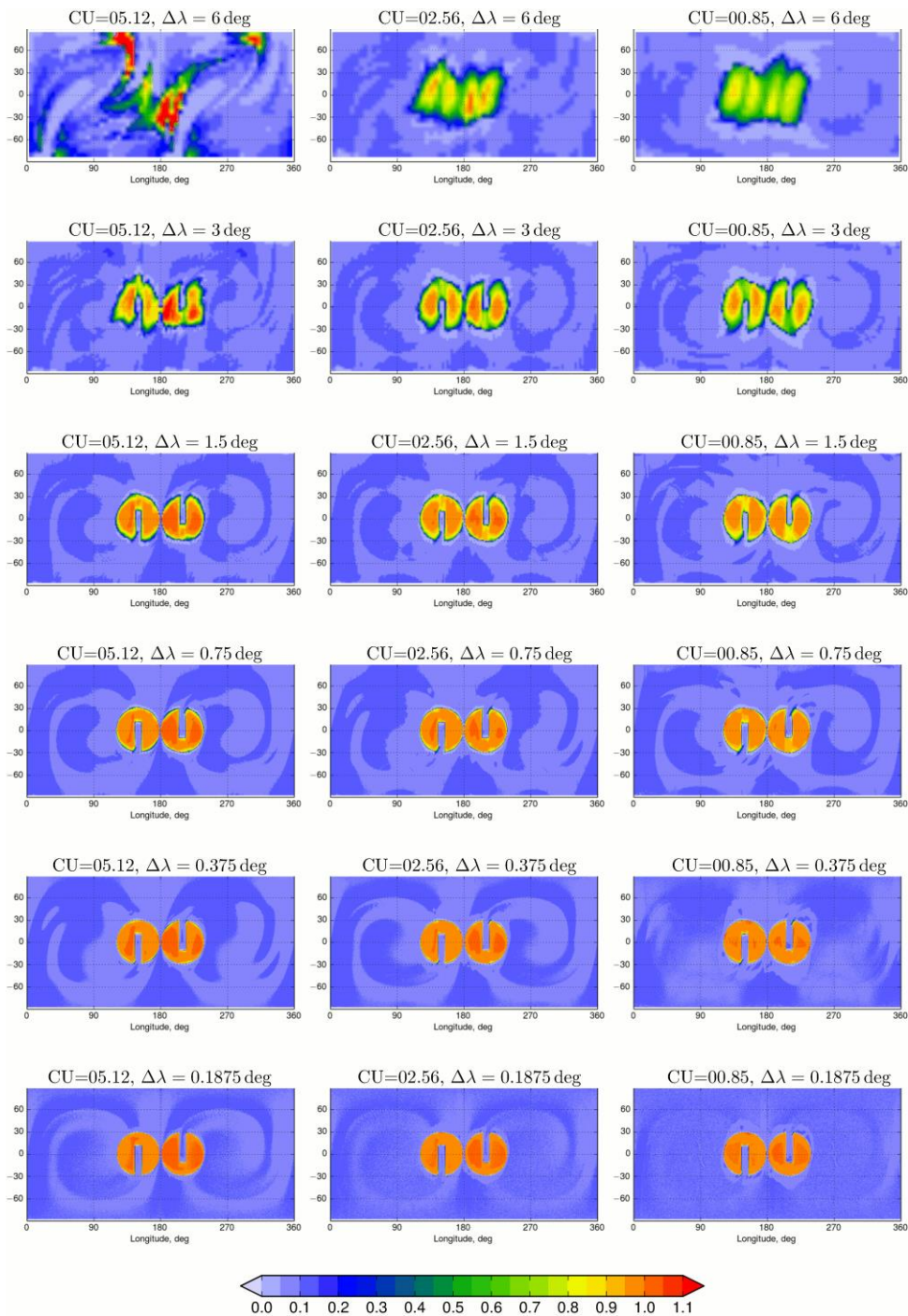


**Figure 10. Final shapes ( $t=T$ ) for the 2-D global tests with slotted cylinders for different spatial and temporal resolutions. Without smoother,**

**Deleted:** Figure 8. Final shapes ( $t=T$ ) for the 2-D global tests with slotted cylinders for different spatial and temporal resolutions

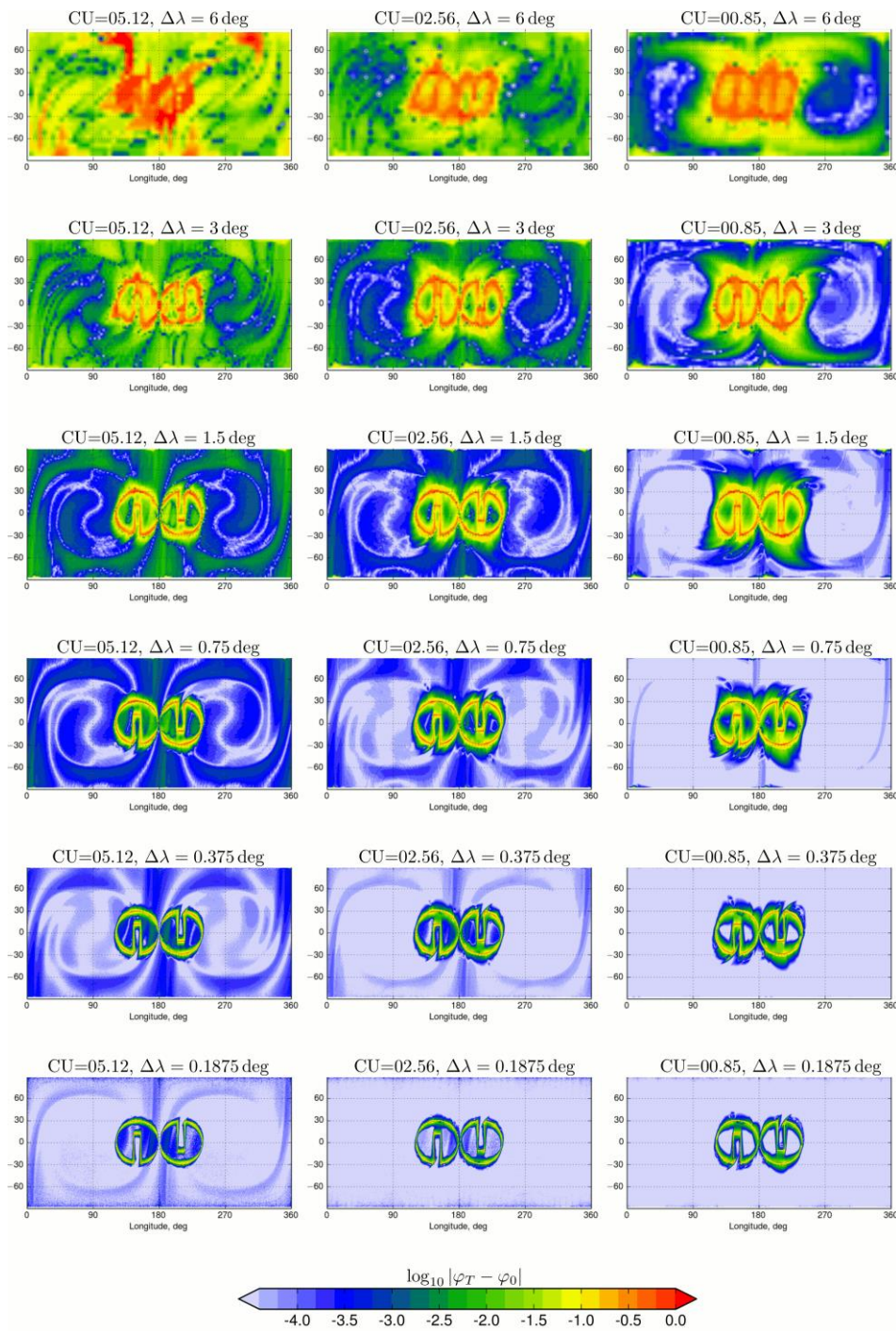


**Figure 11. The error fields for the final shapes of Figure 10 as compared with slotted cylinder initial shape in Figure 8. Without smoother,**

**Deleted:** Figure 9. The error fields for the final shapes of Figure 8 as compared with slotted cylinder initial shape in Figure 6.

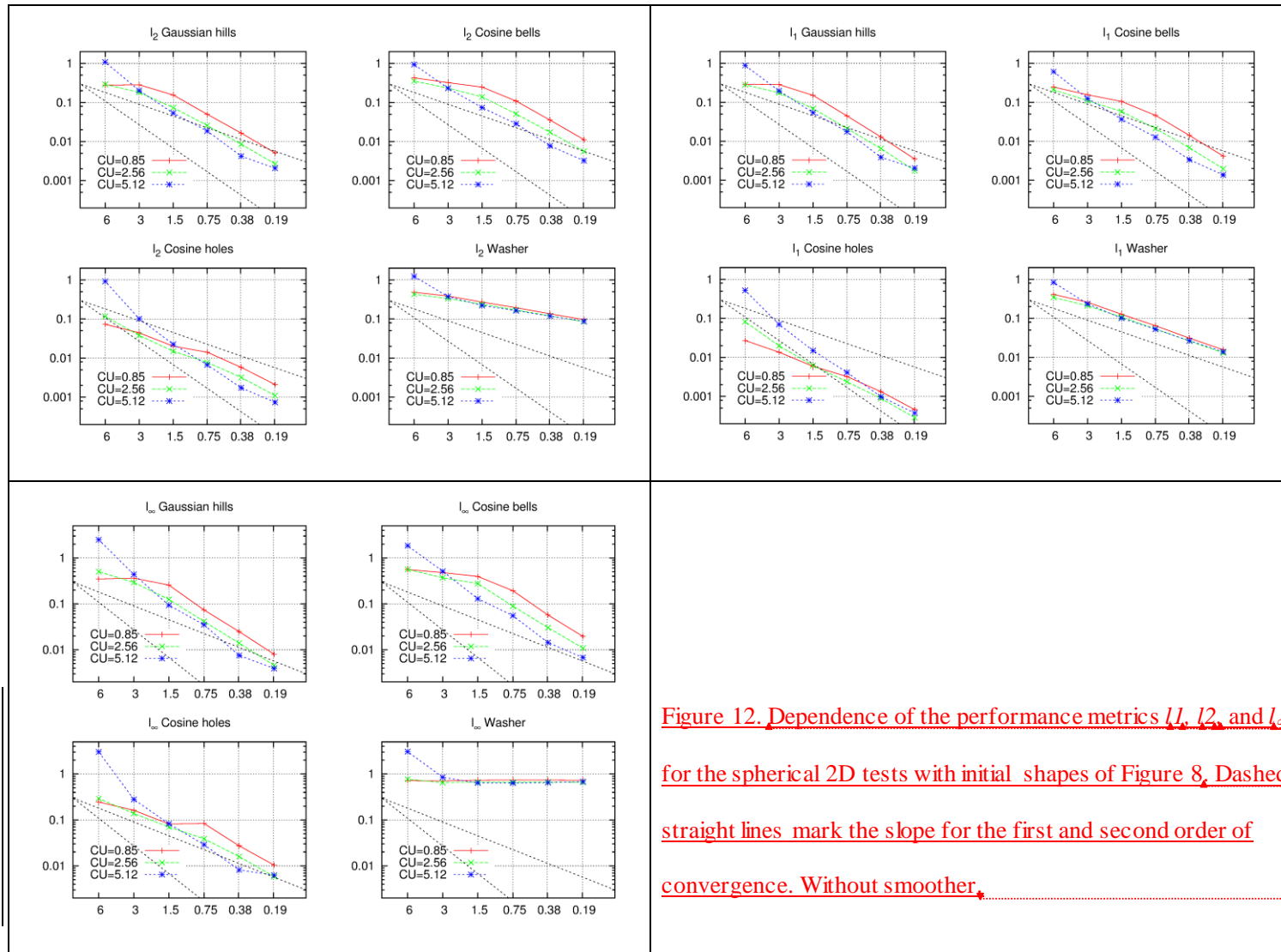


Figure 12. Dependence of the performance metrics  $l_1$ ,  $l_2$ , and  $l_\infty$  for the spherical 2D tests with initial shapes of Figure 8. Dashed straight lines mark the slope for the first and second order of convergence. Without smoother.

**Formatted:** Font:Not Bold

**Formatted:** Font:Not Bold, Not Superscript/Subscript

**Formatted:** Font:Not Bold

**Formatted:** Font:Not Bold, Not Superscript/Subscript

**Formatted:** Font:Not Bold, Italic

**Formatted:** Font:Not Bold

**Formatted:** Font:Not Bold

**Formatted:** Font:Not Bold

**Formatted:** Font:Not Bold, Do not checkspelling or grammar

**Deleted:** Figure 10. Dependence of the performance metrics  $l_1$ ,  $l_2$ , and  $l_\infty$  for the spherical 2D tests with initial shapes of Figure 6. Dashed straight lines mark the slope for the first and second order of convergence.

Scatter plot  $t=T/2$ , v5-ref vs v5-d092

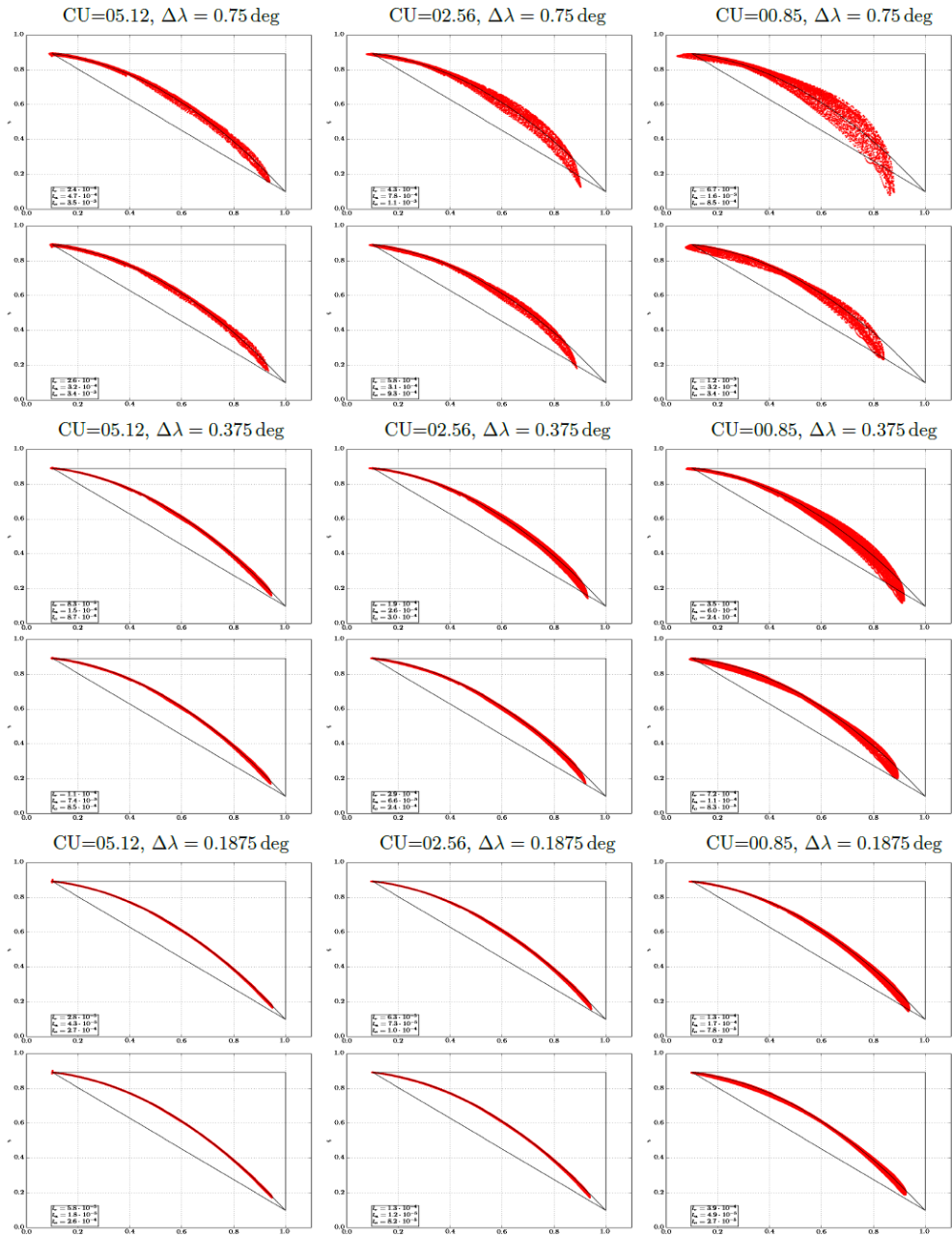


**Figure 13. Mixing preservation test for cosine bells and correlated cosine bells ( 27) at  $t=T/2$ . Each two lines show the tests without (upper line) and with (lower line) smoother ( 20).**

**Deleted:** Figure 11. Linearity test for cosine bells and correlated cosine bells ( 26) at  $t=T/2$ . Each two lines show the tests without (upper line) and with (lower line) smoother ( 20).

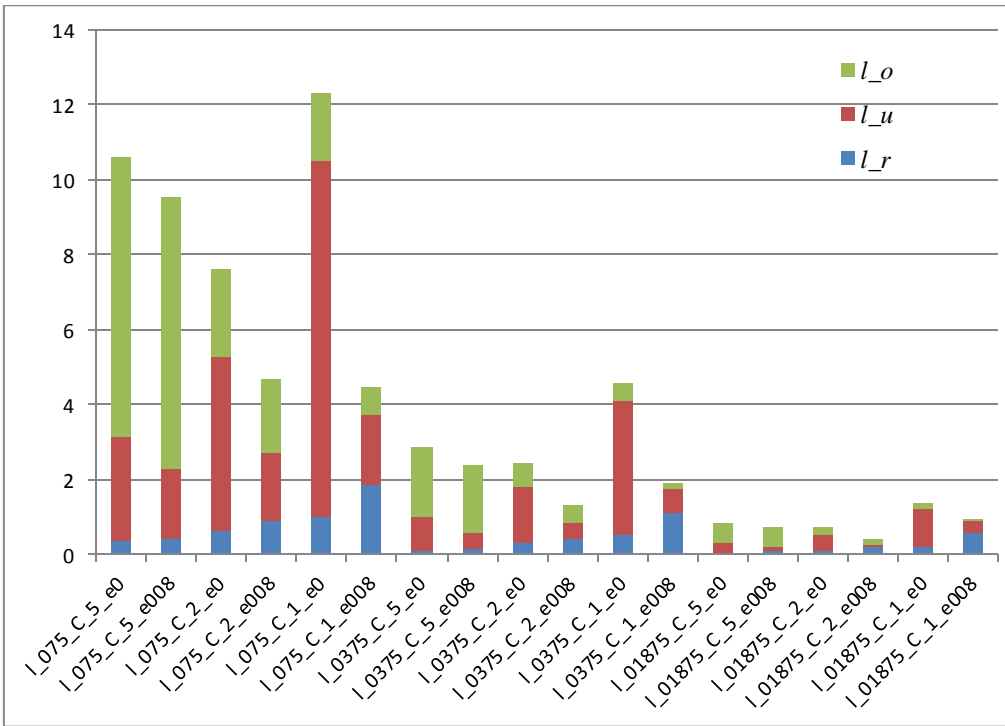


Figure 14. A histogram of mixing diagnostic (stacked) for the same resolutions, Courant number and smoother factor as in Figure 13. Metrics are (see text and (Lauritzen et al. 2012) for more details):  $l_r$  is “real mixing”,  $l_u$  is “range-preserving unmixing”,  $l_o$  is “overshooting”. Values are relative to the reference CSLAM performance in L14 tests. Picture is comparable with panel b) of Fig. 15 in L14.

- Formatted: Font: 11 pt
- Formatted: Font: 11 pt, Not Bold
- Formatted: Font: 11 pt
- Formatted: Font: 11 pt, Not Bold, Do not check spelling or grammar
- Formatted: Font: 11 pt, Not Bold, Not Superscript/ Subscript
- Formatted: Font: 11 pt, Not Bold
- Formatted: Font: 11 pt, Not Bold, Not Superscript/ Subscript
- Formatted: Font: 11 pt, Not Bold
- Formatted: Font: 11 pt, Not Bold, Not Superscript/ Subscript
- Formatted: Font: 11 pt, Not Bold

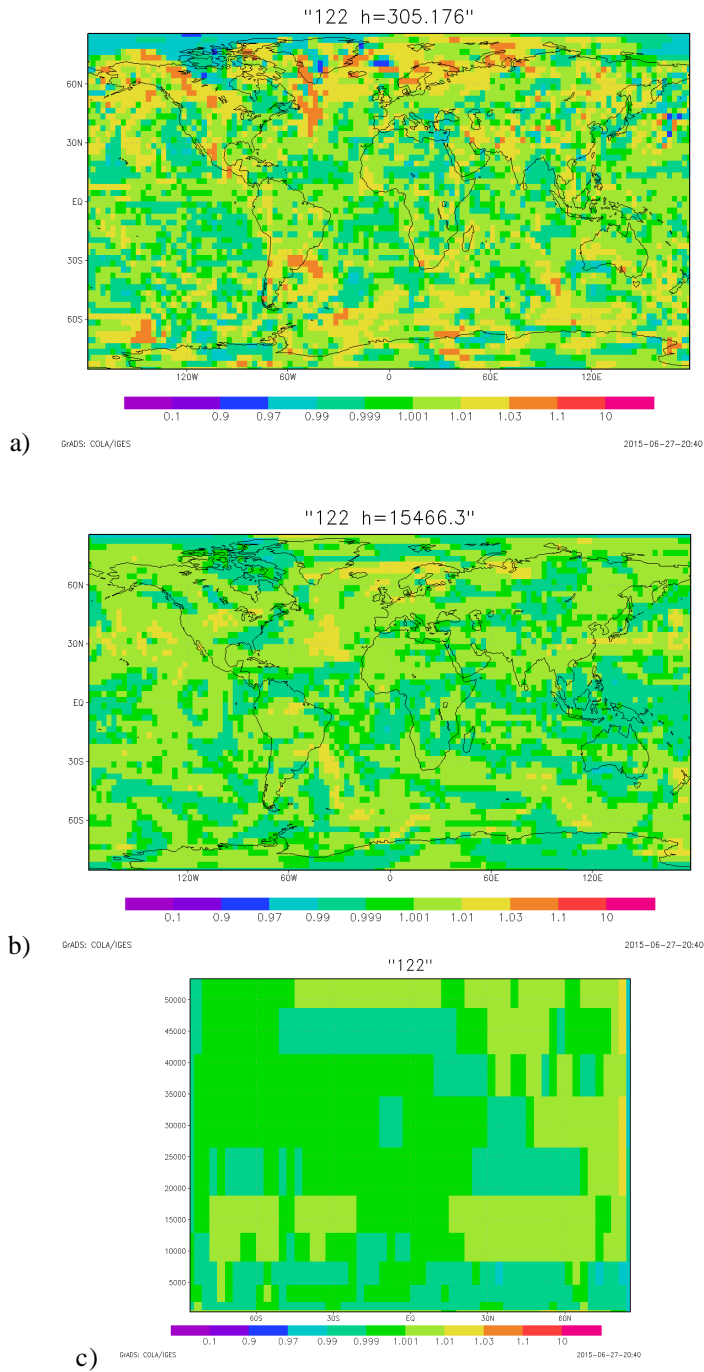
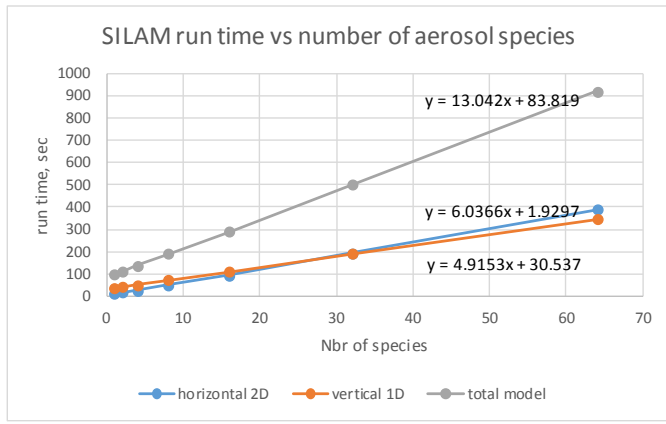


Figure 15. Constant-vmr test with real-wind conditions after 122 hrs. a) vmr within boundary layer, b) vmr above the tropopause, c) zone-average vertical cross-section of vmr. Without smoother.

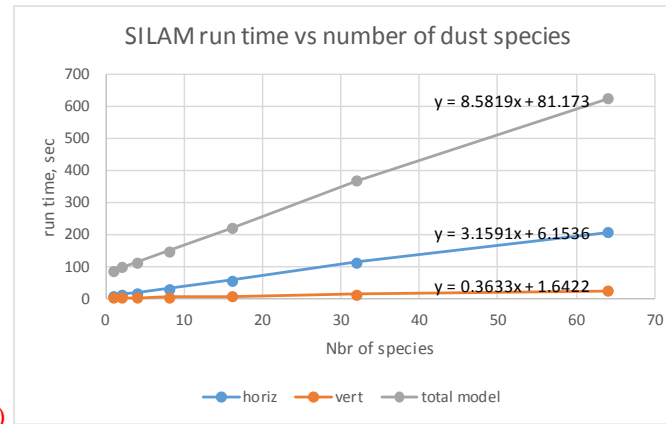
Formatted: Font: Not Bold

Deleted: Figure 12. Constant-vmr test with real-wind conditions after 122 hrs. a) vmr near the surface, b) vmr above the tropopause, c) zone-average vertical cross-section of vmr.

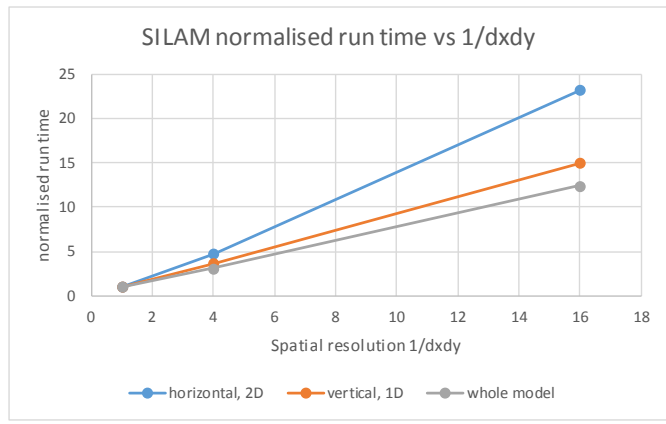
Formatted: Left: 2.54 cm, Right: 2.54 cm, Top: 2.5 cm, Bottom: 2.5 cm, Width: 29.7 cm, Height: 21 cm



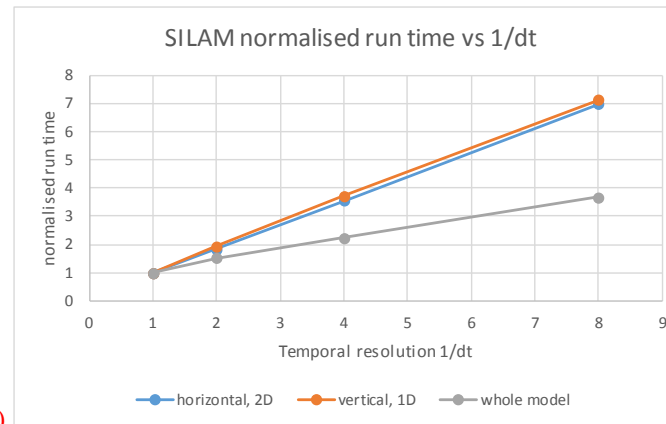
a)



b)



c)



d)

Figure 16. Scalability of Galperin advection scheme and SILAM model. Panel a) Full-grid runtime for different number of species, b) sparse-plume run time for different number of species, c) full-grid run time for varying horizontal grid resolution, d) full-grid run time for varying time step